Retromer subunit, VPS29, regulates synaptic transmission and is required for endolysosomal function in the aging brain

Hui Ye[1], Shamsideen Ojelade[2], David Li-Kroeger[1], Zhongyuan Zuo[1], Liping Wang[3], Yarong Li[2], Jessica Y. J. Gu[4], Ulrich Tepass[4], Avital A. Rodal[5], Hugo J. Bellen[1,3,6,7,8], Joshua M. Shulman[1,2,3,6,8*]

1. Department of Molecular and Human Genetics, Baylor College of Medicine, Houston, TX
2. Department of Neurology, Baylor College of Medicine, Houston, TX
3. Program in Developmental Biology, Baylor College of Medicine, Houston, TX
4. Department of Cell and Systems Biology, University of Toronto, Ontario, Canada
5. Department of Biology, Brandeis University, Waltham, MA
6. Department of Neuroscience, Baylor College of Medicine, Houston, TX
7. Howard Hughes Medical Institute, Houston, TX
8. Jan and Dan Duncan Neurological Research Institute, Texas Children's Hospital, Houston, TX

*Correspondence:
Joshua M. Shulman, MD, PhD
Jan and Dan Duncan Neurological Research Institute
1250 Moursund St., Suite N.1150
Houston, TX 77030
832 824-8976
Joshua.Shulman@bcm.edu

Running Head: VPS29 and neuronal endolysosomal function

Keywords: *VPS29*; *VPS35*; retromer; *Drosophila*; neuron; *TBC1D5*; Rab7 GTPase; endolysosomal pathway

Abstract

Retromer, including Vps35, Vps26, and Vps29, is a protein complex responsible for recycling proteins within the endolysosomal pathway. Although implicated in both Parkinson's and Alzheimer's disease, our understanding of retromer function in the adult brain remains limited, in part because *Vps35* and *Vps26* are essential for development. In *Drosophila*, we find that *Vps29* is dispensable for embryogenesis but required for retromer function in aging adults, including for synaptic transmission, survival, and locomotion. Unexpectedly, in *Vps29* mutants, Vps35 and Vps26 proteins are normally expressed and associated, but retromer is mislocalized from neuropil to soma with the Rab7 GTPase. Further, *Vps29* phenotypes are suppressed by reducing Rab7 or overexpressing the GTPase activating protein, TBC1D5. With aging, retromer insufficiency triggers progressive endolysosomal dysfunction, with ultrastructural evidence of impaired substrate clearance and lysosomal stress. Our results reveal the role of Vps29 in retromer localization and function, highlighting requirements for brain homeostasis in aging.

Impact Statement

Vps29 promotes retromer localization in the adult *Drosophila* brain, engaging Rab7 and TBC1D5, and its loss triggers age-dependent neuronal impairments in endolysosomal trafficking and synaptic transmission.

Introduction

The endolysosomal membrane system comprises a dynamic network of interconnected compartments that mediates sorting or degradation of endocytosed proteins (Klumperman and Raposo, 2014; Repnik et al., 2013). Many factors that regulate endolysosomal trafficking are implicated in human disease, including neurodegenerative disorders (Small and Petsko, 2015; Soukup et al., 2018). Among these, retromer is a complex that recycles selected protein cargoes from the endosome to the *trans*-Golgi network or the plasma membrane (Burd and Cullen, 2014; Lucas and Hierro, 2017). Mutations in *VPS35*—encoding a retromer core protein—are a rare cause of familial Parkinson's disease (Vilariño-Güell et al., 2011; Zimprich et al., 2011), and retromer has also been linked to endocytic trafficking and processing of the Amyloid Precursor Protein and Tau in Alzheimer's disease (Muhammad et al., 2008; Vagnozzi et al., 2019; Wen et al., 2011). Despite its emerging importance in neurodegenerative disease, the requirements of retromer in neurons and particularly within the aging nervous system remain incompletely understood.

Originally discovered in the yeast *S. cerevisiae* (Seaman et al., 1998), the heterotrimeric core proteins of the retromer, VPS35, VPS26, and VPS29, are highly conserved among eukaryotes (Koumandou et al., 2011). Retromer components are broadly expressed, including in the invertebrate nervous system (Inoshita et al., 2017; Wang et al., 2014) and throughout the mammalian brain (Appel et al., 2018; Tsika et al., 2014). In murine neurons, retromer is present in both axons and dendrites, and at the synapse (Munsie et al., 2015; Tsika et al., 2014). Post-synaptically, retromer appears important for trafficking of AMPA, β2 adrenergic, and perhaps other neurotransmitter receptors to the dendritic membrane (Choy et al., 2014; Munsie et al., 2015; Temkin et al., 2017). In rat mesencephalic cultures, retromer also participates in pre-synaptic dopamine transporter trafficking (Wu et al., 2017), and studies of *Vps35* at the *Drosophila* neuromuscular junction are suggestive of a requirement for synaptic vesicle recycling (Inoshita et al., 2017). *Vps35*-deficient mice exhibit both defective hippocampal neurotransmission (Muhammad et al., 2008) and dopaminergic insufficiency (Tang et al., 2015a, 2015b), leading to impairments in memory and locomotion, respectively.

Retromer regulates lysosomal degradation pathways, including autophagy, which are important for quality control and brain homeostasis (Martini-Stoica et al., 2016; Menzies et al., 2015). In the absence of retromer, many protein cargoes are misdirected to the lysosome (Burd and Cullen, 2014; Lucas and Hierro, 2017; Wang and Bellen, 2015), potentially overwhelming degradative capacity, leading to lysosomal expansion and cellular stress. For example, in the *Drosophila* retina, loss-of-function for *Vps35* or *Vps26* results in accumulation of the visual pigment, Rhodopsin-1 (Rh1), within photoreceptors, ultimately causing neuronal dysfunction and loss (Wang et al., 2014). Nevertheless, most investigations of the retromer in lysosomal function have relied on cell culture paradigms using non-neuronal cell types (Cui et al., 2019; Jimenez-Orgaz et al., 2017; Zavodszky et al., 2014). Ablation of *VPS35* in the mouse germline is embryonic lethal (Wen et al., 2011), and both *Vps35* and *Vps26* similarly have essential developmental requirements in *Drosophila* (de Vreede et al., 2014; Franch-Marro et al., 2008; Pocha et al., 2011; Starble and Pokrywka, 2018; Strutt et al., 2019; Wang and Bellen, 2015).

Notably, among the retromer core proteins, the precise roles of each subunit remain incompletely defined, with especially scant data on VPS29. VPS29 binds the VPS35 C-terminus (Collins et al., 2005; Hierro et al., 2007; Kovtun et al., 2018). Deletion of *Vps29* in yeast or *C. elegans* phenocopies *Vps35* loss-of-function (Lorenowicz et al., 2014; Seaman et al., 1997). In mammalian epithelial cell culture, reducing VPS29 results in apparent destabilization and degradation of both VPS35 and VPS26 (Fuse et al., 2015; Jimenez-Orgaz et al., 2017). Reciprocally, pharmacological chaperones targeting the VPS35-VPS29 interface can stabilize the complex and enhance retromer function (Mecozzi et al., 2014; Young et al., 2018). Here, we have generated and characterized a *Drosophila Vps29* null allele with a focus on *in vivo* requirements in the nervous system. We identify an unexpected requirement for Vps29 in the regulation of retromer localization, and further highlight a role in synaptic vesicle recycling and lysosomal function in the aging brain.

Results

Vps29 is required for age-dependent retinal function

Drosophila Vps29 is predicted to encode a 182 amino-acid protein that is 93% similar (83% identical) to human VPS29. Prior studies of *Vps29* in flies have relied on RNA-interference knockdown approaches (Linhart et al., 2014). We instead generated a *Vps29* null allele using a CRISPR-Cas9 strategy (Li-Kroeger et al., 2018). In the resulting mutant, $Vps29^{1}$, the entire coding sequence was replaced by the visible marker gene, y^{wing2+} (**Figure 1A**). Unexpectedly, $Vps29^{1}$ was homozygous viable, whereas both *Vps35* and *Vps26* mutants are lethal. Loss of the *Vps29* genomic sequence in null animals was confirmed by PCR (**Figure 1B**), and we were not able to detect any protein using an anti-Vps29 antibody on western blots from fly head homogenates (**Figure 1C**). Although viable, $Vps29^{1}$ homozygotes are recovered at ratios below Mendelian expectation (**Figure S1A**). We also recovered viable $Vps29^{1}$ animals lacking both maternal and zygotic protein when crossing homozygous females to heterozygous males. Notably, $Vps29^{1}$ mutant flies exhibit a modestly reduced survival (~50-60 days versus ~75 days for controls), and this result was confirmed when $Vps29^{1}$ animals were crossed to the deficiency, *Df(2L)Exel6004* (**Figure 1D**). The reduced survival seen in *Vps29* null animals was also rescued by a 23-kb P[acman] bacterial artificial chromosome (Venken et al., 2009) containing the *Vps29* genomic locus, establishing specificity.

As introduced above, the retromer plays as essential role in the endocytic recycling of Rh1 in the *Drosophila* eye, thereby enabling proper phototransduction (Wang et al., 2014). Consequently, loss of either *Vps35* or *Vps26* leads to aberrant Rh1 trafficking, resulting in lysosomal stress and progressive retinal degeneration. In order to determine if *Vps29* is similarly required, we generated somatic clones of either $Vps29^{1}$ or the $Vps35^{MH20}$ null allele in the fly eye using the *eyeless* (*ey*)-FLP/FRT system (Newsome et al., 2000), and monitored degeneration using electroretinograms (ERGs). Compared with control clones (*FRT40A*), removing either retromer component from photoreceptors disrupted light-induced depolarization in 10-day-old animals; however, the *Vps29* phenotype was less severe than that due to loss of *Vps35* (**Figure 1E, F**). Consistent with other retromer components, the $Vps29^{1}$ retinal degeneration phenotype was suppressed when flies were raised in the dark, which eliminates phototransduction and the concomitant endocytosis of Rh1. Age- and light-dependent retinal degeneration

in the absence of *Vps29* was further confirmed by histology (**Figure S1B**), and this phenotype was also reversed by introduction of the *Vps29* genomic rescue construct (**Figure S1B**). On further inspection of the ERG traces, we noticed that both $Vps29^{1}$ and $Vps35^{MH20}$ appear to disrupt synaptic transmission (**Figure 1E, G**), based on progressive reduction in the on- and off-transient potentials in aging animals (Babcock et al., 2003). Interestingly however, whereas raising animals in the dark rescued phototransduction, the ERG transient phenotypes persisted, suggesting a role for retromer at the synapse that is independent of Rh1 recycling.

In our ERG experiments, we also noticed that whereas the transient potentials are preserved in newly-eclosed *Vps29* or *Vps35* mutant animals, they frequently failed to sustain transient potentials throughout the recordings. We therefore repeated our ERG experiments in $Vps29^{1}$ and $Vps35^{MH20}$ retinae, but instead using a rapid light stimulation paradigm. Indeed, we documented a progressive decline in the on- and off-transient potentials following rapid stimulation (**Figure 1H** & **S1C**), and consistent results were obtained using the $ey^{3.5}$*-FLP* driver (Mehta et al., 2005), which selectively targets presynaptic neurons (**Figure 1H**). This "run-down" phenotype is characteristic of mutants that disrupt synaptic vesicle recycling (Harris and Littleton, 2015), suggesting that retromer is required for this process. We further demonstrated that the *Vps29* retinal synaptic transmission phenotype was fully rescued using the pan-neuronal expression driver (*nSyb-GAL4*) and a full-length *Drosophila Vps29* cDNA (*nSyb >Vps29*) (**Figure 1I**). Finally, similar rescue was observed when expressing 3 alternate human *Vps29* isoforms, suggesting potential functional conservation. Surprisingly, we also found that pan-neuronal overexpression of *Vps35* (*nSyb>Vps35*) partially restored synaptic transmission in $Vps29^{1}$ mutants. In combination with the somewhat weaker phenotype, this result suggests that Vps29 may function primarily to potentiate the activity of other retromer subunits in the retina, such that Vps35 overexpression is compensatory. In sum, whereas Vps29 appears dispensable for retromer function during embryogenesis and development, these studies reveal a requirement in the aging nervous system for phototransduction and synaptic transmission.

Retromer regulates synaptic vesicle endocytosis and recycling

To explore the requirement of retromer at synapses, we next turned to the larval neuromuscular junction (NMJ). Based on previous work, Vps35 is present at both the NMJ pre- and post-synapse, and loss of *Vps35* causes synaptic terminal overgrowth and altered neurophysiology suggestive of synaptic vesicle recycling defects (Inoshita et al., 2017; Korolchuk et al., 2007; Malik et al., 2015; Walsh et al., 2019). We therefore examined whether *Vps29* mutants show similar phenotypes. Indeed, NMJ preparations from $Vps29^{1}$ larvae revealed a modest but significant increase in synaptic bouton numbers, consistent with synaptic overgrowth (**Figure 2A**). However, both amplitude and frequency of NMJ miniature excitatory junction potentials (mEJPs) were unaffected following loss of *Vps29* (**Figure 2B**). Similarly, excitatory junction potentials (EJPs) were also preserved (**Figure 2C**). These results suggest that *Vps29* is neither required for spontaneous nor evoked synaptic vesicle release. However, high frequency stimulation (10 Hz for 10 minutes) provoked a marked synaptic depression at the $Vps29^{1}$ NMJ (**Figure 2D**). These data provide further support for the role of Vps29 in synaptic vesicle recycling.

The NMJ synaptic run-down phenotype is characteristic of mutants causing defective endocytosis (Bellen et al., 2010; Verstreken et al., 2002; Winther et al., 2013). To further investigate if synaptic vesicle endocytosis requires the retromer, we performed dye uptake studies in animals lacking *Vps29* or *Vps35*. Larval preparations were stimulated with potassium chloride in the presence of extracellular buffer containing the fluorescent dye FM 1-43, permitting quantification of endocytic flux (Verstreken et al., 2008). In control animals, FM 1-43 dye was rapidly internalized at the presynaptic membrane. However, NMJs from either $Vps29^{1}$ or $Vps35^{MH20}$ animals significantly reduced FM dye uptake (**Figure 2E** & **S1D**). These results are consistent with models whereby retromer either directly or indirectly supports vesicle recycling at the presynapse.

***Vps29* regulates retromer localization and is required in the aging nervous system**

The requirement of retromer during *Drosophila* embryogenesis has hindered systematic characterization of its function in the adult nervous system, with the exception of studies in the retina relying on clonal

analysis of *Vps35* and *Vps26* (Wang et al., 2014). However, whereas *Vps29* is dispensable for embryonic development, our results (above) establish a largely conserved Vps29 requirement for retromer function in the retina and at the NMJ synapse. We therefore studied *Vps29* null adult animals to further explore retromer requirements in the adult brain. Except for the aforementioned retinal requirement (**Figures 1 and S1**), we did not observe obvious morphological defects or apparent evidence of neurodegeneration in the brains of 45-day-old $Vps29^{1}/Df$ adults based on hematoxylin & eosin staining of paraffin sections (**Figure S2A**). In order to examine nervous system function, we next tested the startle-induced negative geotactic response (climbing) (Davis et al., 2016; Rousseaux et al., 2018). Whereas locomotor behavior was normal in newly-eclosed *Vps29* null adults, climbing ability significantly declined with aging (**Figure 3A**). Locomotor defects were partially rescued by pan-neuronal *Vps29* expression (*nsyb>Vps29*), and human *VPS29* showed comparable rescue activity (**Figure 3B**). These results suggest *Vps29* is required for the maintenance of nervous system function in aging animals.

In prior studies of HeLa cell cultures, *VPS29* knockdown caused reduced levels of both VPS35 and VPS26, likely due to destabilization of the retromer trimer complex and subunit turnover (Fuse et al., 2015; Jimenez-Orgaz et al., 2017). Reciprocally, enhancing interactions between VPS29 and VPS35 promotes retromer stability (Mecozzi et al., 2014; Young et al., 2018). However, Vps35 and Vps26 protein levels were unaffected in *Vps29* null animals, based on western blots from either whole larvae or adult *Drosophila* heads (**Figure 3C & S2B**,**C**), including from 30-day-old animals. Furthermore, we confirmed that Vps35 and Vps26 remain tightly associated in the absence of Vps29, based on coimmunoprecipitation assays (**Figure 3D**). Thus, Vps35-Vps26 complex assembly and stability in the nervous system are preserved in *Drosophila* lacking *Vps29*.

Besides expression and stability, retromer function is tightly regulated by its subcellular localization (Follett et al., 2016; Lucas et al., 2016). We examined retromer expression and localization in the adult fly brain using endogenously-tagged fluorescent protein alleles, encoding either $Vps35^{RFP}$ or $Vps35^{GFP}$ (Koles et al., 2016), as well as $Vps29^{GFP}$ (Figure 1A) fusion proteins. As expected, Vps29 and Vps35 appeared to colocalize, and were broadly expressed in the *Drosophila* brain (**Figure 4A**), including

the antennal lobes and the mushroom body (α-/β- lobes and peduncles) (**Figure 4B**). We confirmed that most of the observed staining in the adult brain, including within neuropil regions, derived from neuronal Vps35, as this signal was lost following neuronal-specific knockdown (**Figure S3A**). However, in *Vps29*^{1} null animals, Vps35 showed a striking redistribution, shifting from neuropil to soma, and forming large perinuclear puncta (**Figure 4C**). Moreover, Vps35 was mislocalized in brains from 1-day-old adults and this result did not significantly change with aging. Our data therefore suggest that Vps29 is required for normal retromer localization within neurons.

Vps29 interacts with *Rab7* and *TBC1D5*

Based on cell culture studies, Vps35 is recruited to endosomal membranes by the Rab7 GTPase (Seaman et al., 2009), and *VPS29* knockdown has been previously suggested to increase GTP-bound, activated Rab7 (Jimenez-Orgaz et al., 2017). We therefore examined whether dysregulation of Rab7 may similarly participate in neuronal retromer localization *in vivo*. Indeed, in the adult brain of *Vps29*^{1} null flies, the Rab7 signal appeared strongly increased and was restricted to a somatic, perinuclear pattern with relative depletion from neuropil (**Figure 4E & S3B**). Moreover, Vps35 strongly co-localized with perinuclear Rab7 (**Figure 4E**). On western blots, we documented an increase in Rab7 protein following loss of *Vps29* (**Figure 4F & S3C**). To examine if the change in Rab7 expression level reflects an altered ratio of GTP-bound (active) to GDP-bound (inactive) Rab7 protein (**Figure 4D**), we leveraged available fly strains harboring Venus-tagged *Rab7* transgenes (Cherry et al., 2013), including wildtype *Rab7*, the "GTP-locked" mutant *Rab7*^{Q67L} and the "GDP-locked" mutant *Rab7*^{T22N}, under the control of identical *Rab7* promoter elements (*Rab7-GAL4*). We found that the constitutively active, GTP-locked Rab7^{Q67L} protein was present at higher levels, and endogenous wildtype Rab7 was also increased (**Figure 4G & S3D**). Overall, these data support a model in which loss of *Vps29* promotes Rab7 activation, redistribution of active Rab7 from axon to soma, and subsequent recruitment of Vps35.

If Rab7 activation mediates the disruption in retromer localization and function in *Vps29* mutants, our model predicts that reduction in Rab7 may rescue the neuronal requirements for Vps29. Indeed,

although complete loss-of-function for *Rab7* is lethal, removing one copy ($Rab7^{Gal4\text{-}KO}/+$) (Cherry et al., 2013) partially rescued the age-dependent locomotor impairment and synaptic transmission defects manifest in $Vps29^{1}/Df$ animals (**Figure 5A-B**). Reduction of *Rab7* also restored synaptic vesicle endocytosis at the larval NMJ based on the FM 1-43 dye uptake assay (**Figure 5C**). In mammalian cell culture studies, VPS29 regulates Rab7 activity via recruitment of the GTPase-activating protein (GAP), TBC1D5 (Jia et al., 2016; Seaman et al., 2009). *Drosophila* has a single ortholog of TBC1D5 that is well-conserved (28% identity / 47% similarity). Consistent with our model, pan-neuronal overexpression of *dTBC1D5* (*nsyb>dTBC1D5*) normalized Rab7 protein levels (**Figure 5D**) and partially rescued the synaptic transmission defect in *Vps29* mutants (**Figure 5E**). Next, using CRISPR-Cas9 (Li-Kroeger et al., 2018), we introduced a point mutation at the *Vps29* genomic locus causing the single amino-acid substitution, $Vps29^{L152E}$ (**Figure 1A**), which has been shown to disrupt the interaction with TBC1D5 in mammalian cells (Jia et al., 2016; Jimenez-Orgaz et al., 2017). $Vps29^{L152E}$ failed to complement $Vps29^{1}$, causing age-dependent photoreceptor synaptic transmission defects and locomotor impairment (**Figure. 5F, 5G, & S4A**). Moreover, $Vps29^{L152E}$ was expressed at higher levels and Rab7 was also increased, as in $Vps29^{1}$ (**Figures S4B & 5H**). Our results suggest that Vps29 regulates retromer localization and function coordinately with Rab7 and TBC1D5.

Loss of *Vps29* causes lysosomal dysfunction during aging

As introduced above, retromer mediates the recycling of protein cargoes from the endolysosomal system to the *trans*-Golgi network or plasma membrane. In the *Drosophila* retina, besides aberrant trafficking of Rh1 (Wang et al., 2014), loss of *Vps35* also causes accumulation of ceramide lipid species (Lin et al., 2018), which contributes to lysosomal expansion, cellular stress, and ultimately photoreceptor loss. We confirmed that glucosylceramide similarly accumulates in *Vps29* mutant photoreceptors (**Figure 6A**), consistent with the retinal degeneration phenotype (**Figures 1 & S1**). In order to better understand the proximal consequences of retromer mislocalization that lead to neuronal dysfunction, we performed a series of experiments to assay lysosomal function in the adult brains of *Vps29* mutants. We first examined

the lysosomal proteases, cathepsin D (CTSD) and cathepsin L (CTSL). These enzymes are each synthesized as propeptides in the endoplasmic reticulum (ER) and become active following cleavage in the acidic, lysosomal milieu. Lysosomal dysfunction therefore commonly leads to reduced levels of mature cathepsins and increased levels of the immature proforms (Hasanagic et al., 2015; Li et al., 2017). We detected normal levels of mature CTSL and increased mature CTSD in adult head homogenates from 1-day-old *Vps29*^{1}*/Df* animals (**Figure 6B & S5A**). However, in 30-day-old animals, we found that the uncleaved proforms of both cathepsins were sharply increased, consistent with progressive lysosomal dysfunction with aging (**Figure 6B & S5A**).

We next examined well-established markers of lysosomal autophagy, which plays a critical role in nervous system homeostasis and neurodegeneration (Martini-Stoica et al., 2016; Menzies et al., 2015). Substrate degradation is triggered when Atg8-decorated autophagosomes fuse with lysosomes, leading to turnover of Ref(2)P/p62 and concomitant clearance of polyubiquitinated proteins. We did not observe any accumulation of these markers in either 1- or 30-day-old *Vps29* mutant brains (**Figure S5B, C**), consistent with preserved autophagic flux. Interestingly however, at more extreme ages (45-days), *Vps29* mutants showed evidence of accelerated autophagic failure, with more significant elevation of both p62 and Atg8, and accumulation of polyubiquitinated proteins (**Figure 6C**). Notably, reduction of *Rab7* (*Rab7*$^{Gal4\text{-}KO}$*/+*) improved autophagic clearance in *Vps29* mutant brains.

Lastly, in order to directly visualize lysosomal ultrastructure, we performed transmission electron microscopy (TEM) on retinae and brains from 30-day-old *Vps29* mutants. For the retinal studies, we selected conditions for which photoreceptor depolarization is preserved **(Figure S6A**), preceding overt retinal neurodegenerative changes. Indeed, retinal TEM revealed normal numbers and morphology of photoreceptors (**Figures 7A & S6B**); however, we documented significantly increased numbers of lysosomes, multivesicular bodies, and autophagic vacuoles (**Figure 7A, B**). Further, lysosomes were frequently aberrantly enlarged and filled with granular, electrodense material (**Figure 7A-C**). These findings are highly suggestive of endolysosomal dysfunction in *Vps29*^{1}*/Df* animals, in agreement with results from other assays (**Figure 6**). Interestingly, although synaptic transmission is disrupted in these

animals (*i.e.* reduced ERG on/off transients in **Figure S6A**), *Vps29* mutant synaptic terminals in the lamina appeared unremarkable (**Figure S6C**). We documented normal synapse numbers and size, nor did we detect any other apparent evidence of synaptic degeneration. Lastly, we examined TEM of adult brain sections in 30-day-old animals, focusing on cortical regions with densely packed neuronal cell bodies in the dorsal-posterior brain (**Figure 7D & S6D**). Consistent with findings in the retina, we discovered significantly increased numbers of aberrant lysosomal structures (multilamellar bodies) in *Vps29* mutants (**Figure 7D**). Collectively, our data indicate that retromer dysfunction following loss of *Vps29* is associated with progressive lysosomal structural and functional degeneration in the aging nervous system.

Discussion

Although strongly implicated in pathogenesis of human neurodegenerative disease, the requirements for retromer in the aging brain remain poorly defined. Our discovery that Vps29 is dispensable for *Drosophila* embryogenesis provides an unexpected opportunity to examine the neuronal consequences of retromer dysfunction *in vivo*. In the absence of *Vps29*, we document age-dependent impairment in lysosomal proteolysis and autophagy, leading to apparent accumulation of undigested substrates and expansion of the endolysosomal compartment. These cellular changes are accompanied by progressive nervous system dysfunction, with synaptic transmission especially vulnerable. Unexpectedly, Vps29 loss did not affect the expression or stability of other retromer components but influenced their localization via a Rab7- and TBC1D5-dependent regulatory pathway.

VPS29 is required for retromer recruitment via Rab7 and TBC1D5

The retromer core initiates cargo recognition and mediates the engagement of other factors that enable proper endocytic trafficking (Cullen and Steinberg, 2018). However, the differential requirements of each protein within the heterotrimer, including VPS35, VPS26, and VPS29, remain incompletely defined. Structural studies suggest the retromer core has an elongated, flexible structure, with VPS35 serving as a

central scaffold, binding VPS26 at its N-terminus, and VPS29 at its C-terminus (Hierro et al., 2007; Kovtun et al., 2018; Lucas et al., 2016). Consistent with this, loss of VPS35 destabilizes the retromer complex, resulting in reduced VPS26 and VPS29 protein, and this result has been confirmed both *in vitro* and *in vivo* (Cui et al., 2019; Liu et al., 2014; Wang et al., 2014). Similarly, knockdown or knockout of *VPS29* in mammalian epithelial cell culture compromises retromer stability, causing loss of the other components (Fuse et al., 2015; Jimenez-Orgaz et al., 2017). Surprisingly, in the absence of Vps29 in *Drosophila*, we found that Vps35 and Vps26 are present at normal levels and remain tightly associated. Instead, Vps35 appears to be mislocalized, shifting from neuropil to soma in the adult brain, and likely disrupting its normal function. Loss of Vps29 also causes apparent hyperactivation (and mislocalization) of Rab7, and a mutation previously shown to disrupt the VPS29-TBC1D5 interaction shows similar phenotypes. Importantly, reduction of Rab7 or overexpression TBC1D5 potently suppresses *Vps29* loss-of-function. Our *in vivo* findings recapitulate a two-step molecular mechanism for retromer recruitment and release in neurons (**Figure 8**). First, the retromer core is recruited to the endosomal membrane by Rab7-GTP, allowing it to participate in cargo recycling. Subsequently, Vps29 engages TBC1D5, which activates GTP hydrolysis of Rab7, thereby releasing retromer from the endosome. We propose that in the absence of Vps29, retromer is trapped at the endosomal membrane in the neuronal cell body, leading to sequestration of functional complexes, and progressive impairment in endocytic trafficking.

The reciprocal interplay and interdependence of retromer and Rab7 that we document in the *Drosophila* nervous system is consistent with prior studies in cell culture (Jimenez-Orgaz et al., 2017; Liu et al., 2012; Seaman et al., 2009). By contrast, the viability of *Vps29* mutants as well as our finding of a more selective, regulatory role for Vps29 in complex localization is unexpected. Unlike the other retromer core subunits, *Vps29* is dispensable for embryogenesis and loss-of-function causes milder retinal phenotypes than *Vps35* or *Vps26*. Moreover, Vps35 overexpression partially rescued selected *Vps29* phenotypes, consistent with a context-dependent, regulatory role. Since Vps35 can weakly bind TBC1D5 (Jia et al., 2016), it may be capable of inactivating Rab7, compensating in part for the absence of Vps29. Our finding that retromer retains some residual activity in flies lacking *Vps29* is reminiscent of results

from *C. elegans* (Lorenowicz et al., 2014). Moreover, in *S. cerevisiase*, interaction of Vps26 and Vps35 are similarly preserved following loss of *Vps29* (Reddy and Seaman, 2001). Importantly, these data suggest that the specific requirement(s) for Vps29—and by extension, retromer activity—may be context dependent, varying with cell-type (*e.g.* neuron) and/or specific cargo (*e.g.* Rh1, ceramides, or others). It is also possible that observed phenotypic differences might relate to Vps29 participation in other endosomal sorting machinery besides retromer, such as the recently described "retriever" (McNally et al., 2017); however, this complex has not yet been studied in *Drosophila*. Although we have found that human *VPS29* is capable of functional substitution in flies, it will be important to determine whether our findings also apply in the mammalian nervous system context.

The retromer and endolysosomal trafficking in neurons

Our characterization of flies lacking *Vps29* points to important roles for retromer in both lysosomal and synaptic homeostasis in neurons, interdependent processes that both require proper endocytic trafficking. Following *Vps29* loss-of-function, we detected evidence of progressive deterioration in lysosomal function in the adult brain, based on markers of cathepsin maturation and autophagic flux. In both cases, lysosomal function was preserved in newly-eclosed animals, but deficits emerged gradually with aging. This result suggests that neurons can initially compensate for retromer insufficiency, whereas adaptive mechanisms may breakdown during aging. Vps35 was strongly mislocalized in 1-day-old animals, suggesting that the manifestation of age-dependent vulnerability likely involves more downstream consequences of retromer dysfunction, such as the accumulation of undigested substrates and resulting lysosomal expansion. Indeed, we found ultrastructural evidence of lysosomal stress in the aged retina and brain, including significantly enlarged lysosomes that were filled with electrodense and/or multilammellar material. Based on evidence from multiple, independent experimental systems, protein and lipid cargoes are expected to accumulate in the late endosome and lysosomes in the absence of retromer activity (Tang et al., 2015a; Wang et al., 2014; Wen et al., 2011). Neuronal compensation may entail increasing capacity for substrate turnover, since we found that mature forms of CTSD and markers of autophagic flux were

increased in young animals (**Figure S5**). It is also possible that the production of critical membrane proteins dependent on retromer for recycling can be boosted, at least temporarily. The initial resilience of the brain to *Vps29* deficiency that we uncover in *Drosophila* is consistent with relative preservation of autophagy following VPS29 knockout in HeLa cells (Jimenez-Orgaz et al., 2017). However, there is ample evidence from animal model studies that aging is accompanied by reduced degradative capacity in neurons, which may ultimately contribute to decompensation and increased proteotoxic stress (Mattson and Magnus, 2006).

We additionally found that *Vps29* is required for synaptic transmission in both the *Drosophila* retina and larval NMJ, producing a phenotype characteristic of other genes that regulate endocytosis and synaptic vesicle recycling (Bellen et al., 2010; Harris and Littleton, 2015). Our results confirm and extend prior studies showing that Vps35 is present at the NMJ, and is similarly required for synaptic structure and function (Inoshita et al., 2017; Korolchuk et al., 2007). Whereas both genes appear similarly required for synaptic vesicle endocytosis, loss of *Vps35* but not *Vps29*, also affected spontaneous NMJ activity, causing increased miniature excitatory junction potentials (Inoshita et al., 2017). This is consistent with our other data suggesting *Vps29* causes overall milder defects. *Vps29* synaptic phenotypes were suppressed by either reduction of Rab7 or overexpression of TBC1D5, similar to our studies of lysosomal phenotypes. Interestingly, ERGs also revealed age-dependent, progressive decline in synaptic transmission. Despite evidence of significant degradation of synaptic function with aging, TEM studies of the *Drosophila* lamina did not reveal overt synaptic structural changes, suggesting a more subtle, predominantly functional defect.

While additional studies will be required to refine our understanding, we consider two non-exclusive models for potential retromer requirement(s) at the synapse. First, retromer may regulate the trafficking of a key factor required for synaptic membrane endocytosis and/or replenishing of the vesicle pool from synaptic endosomes. Second, *Vps29*-related synaptic dysfunction may instead be related, more broadly, to progressive lysosomal dysfunction. In fact, recent studies have linked synaptic endosomes, lysosomes, and autophagosomes to presynaptic proteostasis, including during vesicle recycling and

release (Jin et al., 2018; Wang et al., 2017). For example, another Rab GTPase activating protein, TBC1D24—Skywalker in *Drosophila*—has been shown to regulate synaptic vesicle recycling and quality control via a sorting endosome at NMJ terminals (Fernandes et al., 2014; Uytterhoeven et al., 2011). Interestingly, in the *Drosophila* visual system, we found that raising *Vps29* or *Vps35* mutants in the dark rescued retinal degeneration but not synaptic transmission defects, consistent with an uncoupling of retromer requirements in these two spatially distinct processes. Thus, it is possible—if not likely—that synaptic endolysosomal trafficking and function can be regulated independently from that of the neuronal soma.

In future work, it will be important to further dissect retromer-dependent synaptic mechanisms, including in the mammalian context. Retromer components are present at synaptic terminals in mouse primary neuronal culture (Munsie et al., 2015; Vazquez-Sanchez et al., 2018), and in cortical synaptosome preparations (Tsika et al., 2014). However, functional studies to date have largely focused on the post-synaptic membrane, where evidence supports retromer requirements for trafficking of glutamatergic and adrenergic neurotransmitter receptors (Choy et al., 2014; Tian et al., 2015).

Retromer and neurodegenerative disease

Retromer dysfunction has been linked to pathogenesis of Parkinson's and Alzheimer's disease (Small and Petsko, 2015). In both neurodegenerative disorders, synaptic dysfunction is an early pathologic feature, and lysosomal autophagy is also strongly implicated (Ihara et al., 2012; Wang et al., 2017). Our findings of age-dependent, progressive synaptic and lysosomal dysfunction in the adult brain of *Drosophila* lacking *Vps29* may therefore be relevant for our understanding of retromer in human diseases. In fact, variants at numerous other genetic loci related to endocytic trafficking and synaptic maintenance have been discovered as risk factors for Alzheimer's disease (*BIN1, PICALM, CD2AP, SORL1*) (Karch et al., 2014) and Parkinson's disease (*SNCA, LRRK2, SH3GL2/EndoA*, *RAB7L1*) (Soukup et al., 2018). Genetic links have also recently emerged between Parkinson's disease and lysosomal storage disorders, comprising a heterogeneous group of recessive disorders arising from defects in lysosomal biogenesis

and/or function (Ysselstein et al., 2019). These disorders, which can include neurodegenerative features, are characterized by the accumulation of undigested substrates and lysosomal expansion (*e.g.* glucosylceramide in Gaucher's disease). Importantly, retromer participates in the trafficking of lysosomal hydrolases (Cui et al., 2019; Seaman et al., 1997), and in the absence of *Vps29*, we documented accumulation of glucosylceramides along with ultrastructural evidence of brain lysosomal pathology similar to lysosomal storage disorders. Based on mouse models, synaptic dysfunction may be an early manifestation in lysosomal storage disorders similar to *Vps29* mutant flies (Mitter et al., 2003; Ohara et al., 2004; Sambri et al., 2017). Aberrant lysosomal morphology has also been described in both Alzheimer's and Parkinson's disease models (Giasson et al., 2002; Stokin et al., 2005), and in human postmortem brain (García-Sanz et al., 2018; Piras et al., 2016). Targeting the retromer for therapeutic manipulation in neurodegenerative disease is one promising approach, given the availability of small molecule chaperones that bind Vps29 (Mecozzi et al., 2014; Vagnozzi et al., 2019; Young et al., 2018). However, since the endolysosomal system has many functions, including within neurons and other cell types, it will be essential to pinpoint the specific retromer mechanism(s) responsible for age-related brain diseases.

Materials and Methods

See also comprehensive **Key Resources Table** (end of manuscript file).

Fly stocks and husbandry

A complete list of fly strains used in this study is included in the **Key Resources Table**. Detailed information on experimental genotypes can also be found in figures and figure legends. The *Vps29^{1}* null allele was generated using CRISPR/Cas9-mediated gene replacement, as previously described (Li-Kroeger et al., 2018). Briefly, a dominant marker *ywing^{2+}* flanked by homology arms on each side, along with sgRNA expression plasmids, were injected into embryos expressing Cas9 (*y^{1},w*,M{nos-Cas9.P}ZH-2A*). G0 animals were next crossed to *y w*, and progeny were screened for the presence of the *yellow^{+}* wing marker to identify *Vps29^{1}* (*Vps29$^{ywing2+}$*). Studies of *Vps29* mutant flies used either *Vps29^{1}* homozygotes or the transheterozygous genotype, *Vps29^{1}/Df(2L)Exel6004* (referred to as *Vps29^{1}/Df*). To generate the *Vps29* genomic rescue strain, a 23-kb P[acman] genomic fragment (CH322-128G03) including the *Vps29* locus was injected into *y,w,ΦC31 ; VK33 attP* embryos, followed by selection of F1 transformants. All studies using the transgenic *Vps29* BAC examined the genomic rescue construct (*GR*) in heterozygosity (either *Vps29^{1};GR/+* or *Vps29^{1}/Df;GR/+*).

In order to generate the *Vps29$^{WT.GFP}$* and *Vps29$^{L152E.GFP}$* alleles, we again used the CRISPR/Cas9 gene-replacement system, starting with the *Vps29^{1}* strain. The GFP coding sequence was cloned in-frame and proximal to the *Vps29* cDNA using NEBuilder HiFi DNA Assembly Cloning Kit (NEB). Using Q5 Site-Directed Mutagenesis Kit (NEB), the L152E mutation was introduced to the *GFP::Vps29* plasmid. As above, the *GFP::Vps29* or *GFP::Vps29^{L152E}* constructs were each injected into *y^{1} M{nos-Cas9.P}ZH-2A w*; Vps29^{1}/CyO* flies. G0 flies were crossed to *y w*, and F1 progeny were screened for loss of the *yellow^{+}* marker to establish the *Vps29$^{WT.GFP}$* and *Vps29$^{L152E.GFP}$* strains. The sequence of all CRISPR/Cas9-generated strains were confirmed by genomic PCR followed by Sanger sequencing. Genomic DNA from a single fly was prepared using “squish buffer” (10 mM Tris-Cl pH 8.0, 1 mM EDTA, 25 mM NaCl, and

0.2 mg/ml Proteinase K). Total genomic DNA was extracted using the PureLink Genomic DNA Kit (Thermo Fisher Scientific). PCR primers used for additional confirmation of the *Vps29*^{1} allele (Figure 1B) are listed in the **Key Resources Table**.

As part of this study, we also generated transgenic strains carrying *UAS-dVps29-myc*, *UAS-dTBC1D5-myc*, and *UAS-hVps29-FLAG*. The full-length *Drosophila* Vps29 cDNA (*Drosophila* Genomics Resource Center (DGRC) plasmid: GH25884) was cloned proximal to *c-myc* coding sequencing, using primers *dVps29-myc-F* and *dVps29-myc-R* (**Key Resources Table**). The full-length cDNA for *TBC1D5* (DGRC plasmid: BS16827) was similarly cloned proximal to the *c-myc* coding sequencing using primers *dTBC1D5-myc-F* and *dTBC1D5-myc-R*. The *Vps29-myc* and *TBC1D5-myc* PCR products were each digested with BglII and XbaI restriction enzymes (NEB) and ligated to the *pUAST-attB* vector using T4 ligase (NEB). Plasmids containing FLAG-tagged Human VPS29 cDNAs (OHu00442D, OHu02289D, and OHu05688D, respectively) were obtained from GenScript. For PCR cloning, we used *hVps29-R* along with each of the following: *hVps29-1-F* for hVps29 transcript variant 1 (NM_016226.4), *hVps29-2-F* for hVps29 transcript variant 2 (NM_057180.2), and *hVps29-3-F* for hVps29 transcript variant 3 (NM_001282150.1). PCR products were digested by XhoI and XbaI restriction enzymes (NEB), and then ligated to the *pUAST-attB* vector. The resulting constructs were purified, verified by Sanger DNA sequencing, and injected into *y,w,ΦC31 ; VK33* embryos to generate transgenic flies. The generation of *w;Vps35*$^{TagRFP\text{-}T}$ (*Vps35*^{RFP}) with a Rippase-switchable TagRFP-T to GFP tag was described in Koles et al., 2016. *w;Vps35*^{GFP} was generated by crossing *Vps35*^{RFP} to *bam-Gal4;;UAS-Rippase::PEST @attP2* flies to isolate germline ripouts of the TagRFP-T cassette, leaving a C-terminal EGFP knockin.

All *Drosophila* crosses were raised on molasses-based food at 25 °C unless otherwise noted. To induce neuronal specific knockdown of Vps35^{GFP}, we used the deGradFP system (Caussinus et al., 2012; Nagarkar-Jaiswal et al., 2015). Crosses were established and maintained at 18°C, and following eclosure, adults were shifted to 29°C for 7 days before brain dissection.

Histology and Immunofluorescence

For histology, *Drosophila* heads were fixed in 8% glutaraldehyde (Electron Microscopy Sciences) at 4 °C for 6 days and embedded in paraffin. Frontal (5 μm) sections were cut using a Leica Microtome (RM2245), mounted on slides, and stained with hematoxylin & eosin. For whole mount brain immunostaining, adult fly brains were dissected in 1X PBS and fixed at 4°C overnight in 4% paraformaldehyde in 1X PBS (sc-281692, ChemCruz). Fixed brains were permeabilized with 2% PBST (1X PBS+2% Triton X-100) at 4°C for 20 hours, and then vacuumed (Nalgene) at room temperature for 1 hr. Brains were incubated with the primary antibodies at 4 °C for 2 days, followed by secondary antibody incubation for 1 day at 4 °C, then mounted in RapiClear (SunJin Lab Co.). For NMJ staining, wandering third instar larvae were dissected in Hemolymph-Like 3 (HL3) solution without calcium (110 mM NaCl, 5 mM KCl, 10 mM $NaHCO_3$, 10 mM $MgCl_2$, 5 mM trehalose, 30 mM sucrose, and 5 mM HEPES, pH 7.2), fixed in 100% methanol at room temperature for 20 minutes, washed in 0.3 % PBST, and blocked for 1 h in 0.3 % PBST containing 5% normal goat serum. Tissues were incubated with primary antibody overnight at 4°C, followed by secondary antibodies at room temperature for 2 h, and mounted using Vectashield (Vector Laboratories) prior to imaging. All NMJ studies focused on muscles 6/7, abdominal section 2 and 3. For fly retina staining, fly heads were fixed after the removal of proboscis in 3.7% formaldehyde in PBS at 4°C overnight. Fixed retinae were dissected and blocked in 0.1% PBST containing 5% natural donkey serum at room temperature for 1 hour, followed by primary antibody incubation for 2 days at 4°C and secondary antibody incubation for 2 h at room temperature. Primary antibodies were used at following dilutions in 0.3% PBST: FITC-conjugated anti-GFP (sc-9996 FITC, 1:100, Santa Cruz Biotechnology), Mouse anti-Rab7 (1:100, DSHB), Rat anti-Elav (7E8A10,1:500, DSHB), Rabbit anti-GlcCer (1:250, Glycobiotech); Cy3-conjugated anti-HRP (1:150, Jackson ImmunoResearch). For secondary antibodies, we used Cy3-conjugated goat anti-mouse or anti-Rat IgG (1:500, Jackson ImmunoResearch). Confocal microscopy images were acquired with a Model LSM 880 confocal system (Carl Zeiss).

Western blot analysis and Immunoprecipitation

For western blots, adult fly heads or whole larvae were homogenized in 2X Laemmli Sample Buffer (Bio-Rad) with 5% β-mercaptoethanol (Calbiochem) using a pestle (Argos Technologies). The lysates were heated at 95 °C for 5 min, followed by centrifugation at 21,130 × *g* at 4 °C for 15 min before SDS-PAGE analysis. Samples were loaded into 12% Bis-Tris gels (Invitrogen), separated by SDS-PAGE. For immunoprecipitation of $Vps35^{GFP}$, 300 fly heads from 1~2-day-old animals were homogenized on ice in 700 µL of lysis buffer containing 10 mM Tris pH 7.5, 150 mM NaCl, 0.5 mM EDTA, 0.5% NP-40, and 1X complete protease inhibitor (Roche). Homogenized samples were centrifugated at 21,130 × *g* for 30 min at 4°C. 3% (by volume) of the supernatant were reserved for total protein input. The remaining supernatant was incubated for 1 hour at 4°C with 50 µL of protein A/G agarose slurry (Thermo Fisher) to reduce non-specific binding. Following pre-clearing, the lysate was incubated for 3 hours at 4°C with 35 µL of GFP-Trap agarose beads (Allele Biotechnology) with mild agitation. The beads were washed 3 times with lysis buffer, boiled in 70 µL of 2X Laemmli sample buffer (Biorad), and subjected to SDS-PAGE (BOLT12% Bis-Tris Gel, Invitrogen). Gels were transferred to PVDF membrane (Millipore), and blocked in 5% bovine serum albumin (Sigma) in 1X TBST (Tris-buffered saline + 0.1% Tween-20). We used the following primary antibodies and dilutions: mouse anti-tubulin (DM1A, Sigma Aldrich), 1:1000; mouse anti-Rab7 (DSHB), 1:1000; Goat anti-Vps29 (LS-C55674, LifeSpan Biosciences),1:2000; Guinea pig anti-Vps26 (Wang et al., 2014), 1:2000; Guinea pig anti-Vps35 (see below), 1:2000; Mouse anti-CTSL (clone 193702, MAB22591, R&D Systems), 1:2000; Goat anti-CTSD (sc-6487, Santa Cruz): 1:500, Rabbit anti-p62/Ref(2)p (Rui et al., 2015), 1:2000; Rabbit anti-Atg8 (Castillo-Quan et al., 2016), 1:1000; Mouse anti-GFP (B-2, Santa Cruz), 1:1000; Mouse anti-actin (C4, Millipore), 1:1000; Mouse anti-Polyubiquitinylated proteins (clone FK1, Enzo), 1:1000. HRP-conjugated secondary antibodies were used at 1:5000. Antibodies against *Drosophila* Vps35 were generated by immunization of guinea pigs with a bacterially expressed peptide comprising the C-terminal 338 amino acids of Vps35. Bacterial expression as a GST fusion protein was facilitated by the pGEX 6P-2 vector. The GST tag was used for

protein purification and was cleaved off using PreScission Protease (GE Healthcare Life Sciences) prior to immunization.

Survival and climbing assays

For survival analyses, around 200 flies per genotype (approximately equal numbers of females and males) were aged in groups of no more than 30 flies per vial, transferring to fresh vials and food every 2-3 days. For the startle-induced negative geotaxis assay (climbing), 4-5 groups consisting of approximately 15 flies each were placed in a plastic cylinder. Flies were gently tapped to the bottom of the cylinder, and locomotor activity was videotaped and quantified as the percentage of animals climbing past the 9 cm line within a 15 second interval.

Electroretinogram (ERG)

All crosses were initially maintained in the dark to prevent flies from being exposed to light before eclosion. Newly-eclosed adults were either shifted to a 12-h light/dark cycle (3,000 lux for light exposure) or maintained in light-sealed boxes for constant darkness. During aging, the positions of light-exposed vials were randomly shuffled within racks. ERG recordings were performed as previously described (Chouhan et al., 2016). In brief, adult flies were anesthetized and glued to a glass slide, with electrodes placed on the corneal surface and the thorax. Flies were maintained in the dark for at least 1 min prior to stimulation using a train of alternating light/dark pulses. Retinal responses were recorded and analyzed using LabChart software (ADInstruments). At least 8 flies were examined for each genotype and timepoint.

NMJ electrophysiology and FM 1-43 dye studies

Animals were dissected at the wandering third instar stage in HL3 buffer (above), without addition of calcium. Electrophysiologic recordings were performed with 0.5 mM extracellular Ca^{2+} buffer concentrations, as described in Ojelade et al., 2019. Larval motor axons were severed and miniature

excitatory junction potentials (mEJPs) were recorded from muscle 6 of abdominal segments A2 and A3 for 2 mins. EJPs were evoked at 0.2 Hz. EJPs and mEJPs were analyzed using pClamp6 (Molecular Devices) and Mini Analysis Program (Synaptosoft) software, respectively. High frequency stimulation was recorded at 10 Hz for 10 minutes. The recorded EJP data were binned at 0.5-min intervals and normalized to the average EJP. EJP amplitudes were corrected for nonlinear summation as previously described (Martin, 1955). The FM 1-43 dye uptake assay as performed as described in Verstreken et al., 2008. Larval NMJ preparations were stimulated for 2 min in dark conditions using HL3 buffer containing 90mM K^+, 1.5mM Ca^{2+}, and 4 µM FM 1-43 dye. Larval preparations were subsequently washed 5 times with HL3 solution (without 90mM K^+ and calcium), and FM dye uptake was imaged using a Leica Sp8 confocal system. Signal intensity of FM dye per bouton was normalized to each bouton area. Six boutons were sampled per animal. For each genotype, 7-11 animals were assayed.

Transmission Electron Microscopy (TEM)

For analysis of adult eye ultrastructure, fly heads were dissected by removing proboscis and air sacs, then severed from the thorax. For analysis of central brain ultrastructure, fly heads were dissected by removing cuticles and eyes to ensure complete penetration of fixative, leaving each head affixed to the thorax. All samples were processed for TEM as previously described (Chouhan et al., 2016) using a Ted Pella Bio Wave processing microwave with vacuum attachment. Briefly, dissected samples were fixed (4% paraformaldehyde, 2% glutaraldehyde, and 0.1 M sodium cacodylate, pH 7.2) at 4°C for 48 hours, and then submerged in 1% osmium tetroxide for 45 minutes. The fixed samples were dehydrated using an ethanol series followed by propylene oxide, and then embedded using Embed-812 resin (EMS). For brain samples, each head was removed carefully from the thorax prior to embedding. Transverse sections of brains (50 nm) and tangential sections of eyes (50 nm) were prepared with a Leica UC7 microtome, and post-stained with 1% uranyl acetate and 2.5% lead citrate. All TEM images were acquired using a JEOL 1010 Transmission Electron Microscope. TEM images of photoreceptor sections were prepared from 3 different animals per genotype. TEM images of brain sections were prepared from 4 animals per

genotype. Images were acquired from the dorsal-posterior cortical brain region (Figure S6D), including at least 50 cells per brain.

Quantification and Statistics

Confocal images were processed and analyzed using ImageJ software (NIH). Sample size for all comparisons is included in each figure legend (also noted above). For statistical analysis, we performed two-tailed, unpaired t-tests or Analysis of Variance (ANOVA) followed by Tukey's post-hoc test for multiple comparisons, as specified in all figure legends. The significance threshold for all analyses was set to $p < 0.05$. Otherwise, results are noted as "not significant" (n.s.). Error bars in all analyses represent the standard error of the mean (SEM).

References

Appel JR, Ye S, Tang F, Sun D, Zhang H, Mei L, Xiong WC. 2018. Increased microglial activity, impaired adult hippocampal neurogenesis, and depressive-like behavior in microglial VPS35-depleted mice. *J Neurosci* **38**:5949–5968. doi:10.1523/JNEUROSCI.3621-17.2018

Babcock MC, Stowers RS, Leither J, Goodman CS, Pallanck LJ. 2003. A genetic screen for synaptic transmission mutants mapping to the right arm of chromosome 3 in Drosophila. *Genetics* **165**:171–83.

Bellen HJ, Tong C, Tsuda H. 2010. 100 years of Drosophila research and its impact on vertebrate neuroscience: A history lesson for the future. *Nat Rev Neurosci* **11**:514–522. doi:10.1038/nrn2839

Burd C, Cullen PJ. 2014. Retromer: A master conductor of endosome sorting. *Cold Spring Harb Perspect Biol* **6**. doi:10.1101/cshperspect.a016774

Caussinus E, Kanca O, Affolter M. 2012. Fluorescent fusion protein knockout mediated by anti-GFP nanobody. *Nat Struct Mol Biol* **19**:117–122. doi:10.1038/nsmb.2180

Cherry S, Jin EJ, Özel MN, Lu Z, Agi E, Wang D, Jung WH, Epstein D, Meinertzhagen IA, Chan CC,

Robin Hiesinger P. 2013. Charcot-Marie-Tooth 2B mutations in rab7 cause dosage-dependent neurodegeneration due to partial loss of function. *Elife* **2013**. doi:10.7554/eLife.01064.001

Chouhan AK, Guo C, Hsieh YC, Ye H, Senturk M, Zuo Z, Li Y, Chatterjee S, Botas J, Jackson GR, Bellen HJ, Shulman JM. 2016. Uncoupling neuronal death and dysfunction in Drosophila models of neurodegenerative disease. *Acta Neuropathol Commun* **4**:62. doi:10.1186/s40478-016-0333-4

Choy RWY, Park M, Temkin P, Herring BE, Marley A, Nicoll RA, Von Zastrow M. 2014. Retromer mediates a discrete route of local membrane delivery to dendrites. *Neuron* **82**:55–62. doi:10.1016/j.neuron.2014.02.018

Collins BM, Skinner CF, Watson PJ, Seaman MNJ, Owen DJ. 2005. Vps29 has a phosphoesterase fold that acts as a protein interaction scaffold for retromer assembly. *Nat Struct Mol Biol* **12**:594–602. doi:10.1038/nsmb954

Cui Y, Carosi JM, Yang Z, Ariotti N, Kerr MC, Parton RG, Sargeant TJ, Teasdale RD. 2019. Retromer has a selective function in cargo sorting via endosome transport carriers. *J Cell Biol* **218**:615–631. doi:10.1083/jcb.201806153

Cullen PJ, Steinberg F. 2018. To degrade or not to degrade: mechanisms and significance of endocytic recycling. *Nat Rev Mol Cell Biol* **19**:679–696. doi:10.1038/s41580-018-0053-7

Davis MY, Trinh K, Thomas RE, Yu S, Germanos AA, Whitley BN, Sardi SP, Montine TJ, Pallanck LJ. 2016. Glucocerebrosidase Deficiency in Drosophila Results in α-Synuclein-Independent Protein Aggregation and Neurodegeneration. *PLoS Genet* **12**. doi:10.1371/journal.pgen.1005944

de Vreede G, Schoenfeld JD, Windler SL, Morrison H, Lu H, Bilder D. 2014. The Scribble module regulates retromer-dependent endocytic trafficking during epithelial polarization. *Dev* **141**:2796–2802. doi:10.1242/dev.105403

Fernandes AC, Uytterhoeven V, Kuenen S, Wang YC, Slabbaert JR, Swerts J, Kasprowicz J, Aerts S, Verstreken P. 2014. Reduced synaptic vesicle protein degradation at lysosomes curbs TBC1D24/sky-induced neurodegeneration. *J Cell Biol* **207**:453–462. doi:10.1083/jcb.201406026

Follett J, Bugarcic A, Yang Z, Ariotti N, Norwood SJ, Collins BM, Parton RG, Teasdale RD. 2016.

Parkinson disease-linked Vps35 R524W mutation impairs the endosomal association of retromer and induces α-synuclein aggregation. *J Biol Chem* **291**:18283–18298. doi:10.1074/jbc.M115.703157

Franch-Marro X, Wendler F, Guidato S, Griffith J, Baena-Lopez A, Itasaki N, Maurice MM, Vincent JP. 2008. Wingless secretion requires endosome-to-Golgi retrieval of Wntless/Evi/ Sprinter by the retromer complex. *Nat Cell Biol* **10**:170–177. doi:10.1038/ncb1678

Fuse A, Furuya N, Kakuta S, Inose A, Sato M, Koike M, Saiki S, Hattori N. 2015. VPS29-VPS35 intermediate of retromer is stable and may be involved in the retromer complex assembly process. *FEBS Lett* **589**:1430–1436. doi:10.1016/j.febslet.2015.04.040

García-Sanz P, Orgaz L, Fuentes JM, Vicario C, Moratalla R. 2018. Cholesterol and multilamellar bodies: Lysosomal dysfunction in GBA-Parkinson disease. *Autophagy* **14**:717–718. doi:10.1080/15548627.2018.1427396

Giasson BI, Duda JE, Quinn SM, Zhang B, Trojanowski JQ, Lee VMY. 2002. Neuronal α-synucleinopathy with severe movement disorder in mice expressing A53T human α-synuclein. *Neuron* **34**:521–533. doi:10.1016/S0896-6273(02)00682-7

Gramates LS, Marygold SJ, Dos Santos G, Urbano JM, Antonazzo G, Matthews BB, Rey AJ, Tabone CJ, Crosby MA, Emmert DB, Falls K, Goodman JL, Hu Y, Ponting L, Schroeder AJ, Strelets VB, Thurmond J, Zhou P, Perrimon N, Gelbart SR, Extavour C, Broll K, Zytkovicz M, Brown NH, Attrill H, Costa M, Fexova S, Jones T, Larkin A, Millburn GH, Staudt N, Kaufman T, Grumbling GB, Cripps R, Werner-Washburne M, Baker P. 2017. FlyBase at 25: Looking to the future. *Nucleic Acids Res* **45**:D663–D671. doi:10.1093/nar/gkw1016

Harris KP, Littleton JT. 2015. Transmission, development, and plasticity of synapses. *Genetics* **201**:345–375. doi:10.1534/genetics.115.176529

Hasanagic M, Van Meel E, Luan S, Aurora R, Kornfeld S, Eissenberg JC. 2015. The lysosomal enzyme receptor protein (LERP) is not essential, but is implicated in lysosomal function in Drosophila melanogaster. *Biol Open* **4**:1316–1325. doi:10.1242/bio.013334

Hierro A, Rojas AL, Rojas R, Murthy N, Effantin G, Kajava A V., Steven AC, Bonifacino JS, Hurley JH.

2007. Functional architecture of the retromer cargo-recognition complex. *Nature* **449**:1063–1067. doi:10.1038/nature06216

Ihara Y, Morishima-Kawashima M, Nixon R. 2012. The ubiquitin-proteasome system and the autophagic-lysosomal system in Alzheimer disease. *Cold Spring Harb Perspect Med* **2**. doi:10.1101/cshperspect.a006361

Inoshita T, Arano T, Hosaka Y, Meng H, Umezaki Y, Kosugi S, Morimoto T, Koike M, Chang HY, Imai Y, Hattori N. 2017. Vps35 in cooperation with LRRK2 regulates synaptic vesicle endocytosis through the endosomal pathway in Drosophila. *Hum Mol Genet* **26**:2933–2948. doi:10.1093/hmg/ddx179

Jia D, Zhang JS, Li F, Wang J, Deng Z, White MA, Osborne DG, Phillips-Krawczak C, Gomez TS, Li H, Singla A, Burstein E, Billadeau DD, Rosen MK. 2016. Structural and mechanistic insights into regulation of the retromer coat by TBC1d5. *Nat Commun* **7**. doi:10.1038/ncomms13305

Jimenez-Orgaz A, Kvainickas A, Nägele H, Denner J, Eimer S, Dengjel J, Steinberg F. 2018. Control of RAB 7 activity and localization through the retromer-TBC1D5 complex enables RAB 7-dependent mitophagy . *EMBO J* **37**:235–254. doi:10.15252/embj.201797128

Jin EJ, Kiral FR, Ozel MN, Burchardt LS, Osterland M, Epstein D, Wolfenberg H, Prohaska S, Hiesinger PR. 2018. Live Observation of Two Parallel Membrane Degradation Pathways at Axon Terminals. *Curr Biol* **28**:1027-1038.e4. doi:10.1016/j.cub.2018.02.032

Karch CM, Cruchaga C, Goate AM. 2014. Alzheimer's disease genetics: From the bench to the clinic. *Neuron* **83**:11–26. doi:10.1016/j.neuron.2014.05.041

Klumperman J, Raposo G. 2014. The complex ultrastructure of the endolysosomal system. *Cold Spring Harb Perspect Biol* **6**. doi:10.1101/cshperspect.a016857

Koles K, Yeh AR, Rodal AA. 2016. Tissue-specific tagging of endogenous loci in Drosophila melanogaster. *Biol Open* **5**:83–89. doi:10.1242/bio.016089

Korolchuk VI, Schütz MM, Gómez-Llorente C, Rocha J, Lansu NR, Collins SM, Wairkar YP, Robinson IM, O'Kane CJ. 2007. Drosophila Vps35 function is necessary for normal endocytic trafficking and

actin cytoskeleton organisation. *J Cell Sci* **120**:4367–4376. doi:10.1242/jcs.012336

Koumandou VL, Klute MJ, Herman EK, Nunez-Miguel R, Dacks JB, Field MC. 2011. Evolutionary reconstruction of the retromer complex and its function in Trypanosoma brucei. *J Cell Sci* **124**:1496–1509. doi:10.1242/jcs.081596

Kovtun O, Leneva N, Bykov YS, Ariotti N, Teasdale RD, Schaffer M, Engel BD, Owen DJ, Briggs JAG, Collins BM. 2018. Structure of the membrane-assembled retromer coat determined by cryo-electron tomography. *Nature* **561**:561–564. doi:10.1038/s41586-018-0526-z

Li-Kroeger D, Kanca O, Lee PT, Cowan S, Lee MT, Jaiswal M, Salazar JL, He Y, Zuo Z, Bellen HJ. 2018. An expanded toolkit for gene tagging based on MiMIC and scarless CRISPR tagging in Drosophila. *Elife* **7**. doi:10.7554/eLife.38709

Li C, Brazill JM, Liu S, Bello C, Zhu Y, Morimoto M, Cascio L, Pauly R, Diaz-Perez Z, Malicdan MC V., Wang H, Boccuto L, Schwartz CE, Gahl WA, Boerkoel CF, Zhai RG. 2017. Spermine synthase deficiency causes lysosomal dysfunction and oxidative stress in models of Snyder-Robinson syndrome. *Nat Commun* **8**. doi:10.1038/s41467-017-01289-7

Lin G, Lee PT, Chen K, Mao D, Tan KL, Zuo Z, Lin WW, Wang L, Bellen HJ. 2018. Phospholipase PLA2G6, a Parkinsonism-Associated Gene, Affects Vps26 and Vps35, Retromer Function, and Ceramide Levels, Similar to α-Synuclein Gain. *Cell Metab* **28**:605-618.e6. doi:10.1016/j.cmet.2018.05.019

Linhart R, Wong SA, Cao J, Tran M, Huynh A, Ardrey C, Park JM, Hsu C, Taha S, Peterson R, Shea S, Kurian J, Venderova K. 2014. Vacuolar protein sorting 35 (Vps35) rescues locomotor deficits and shortened lifespan in Drosophila expressing a Parkinson's disease mutant of Leucine-rich repeat kinase 2 (LRRK2). *Mol Neurodegener* **9**:23. doi:10.1186/1750-1326-9-23

Liu TT, Gomez TS, Sackey BK, Billadeau DD, Burd CG. 2012. Rab GTPase regulation of retromer-mediated cargo export during endosome maturation. *Mol Biol Cell* **23**:2505–2515. doi:10.1091/mbc.E11-11-0915

Liu W, Tang FL, Erion J, Xiao H, Ye J, Xiong WC. 2014. Vps35 haploinsufficiency results in

degenerative-like deficit in mouse retinal ganglion neurons and impairment of optic nerve injury-induced gliosis. *Mol Brain* **7**:10. doi:10.1186/1756-6606-7-10

Lorenowicz MJ, Macurkova M, Harterink M, Middelkoop TC, de Groot R, Betist MC, Korswagen HC. 2014. Inhibition of late endosomal maturation restores Wnt secretion in Caenorhabditis elegans vps-29 retromer mutants. *Cell Signal* **26**:19–31. doi:10.1016/j.cellsig.2013.09.013

Lucas M, Gershlick DC, Vidaurrazaga A, Rojas AL, Bonifacino JS, Hierro A. 2016. Structural Mechanism for Cargo Recognition by the Retromer Complex. *Cell* **167**:1623-1635.e14. doi:10.1016/j.cell.2016.10.056

Lucas M, Hierro A. 2017. Retromer. *Curr Biol* **27**:R687–R689. doi:10.1016/j.cub.2017.05.072

Malik BR, Godena VK, Whitworth AJ. 2015. VPS35 pathogenic mutations confer no dominant toxicity but partial loss of function in Drosophila and genetically interact with parkin. *Hum Mol Genet* **24**:6106–6117. doi:10.1093/hmg/ddv322

Martin AR. 1955. A further study of the statistical composition of the end-plate potential. *J Physiol* **130**:114–122. doi:10.1113/jphysiol.1955.sp005397

Martini-Stoica H, Xu Y, Ballabio A, Zheng H. 2016. The Autophagy-Lysosomal Pathway in Neurodegeneration: A TFEB Perspective. *Trends Neurosci* **39**:221–234. doi:10.1016/j.tins.2016.02.002

Mattson MP, Magnus T. 2006. Ageing and neuronal vulnerability. *Nat Rev Neurosci* **7**:278–294. doi:10.1038/nrn1886

McNally KE, Faulkner R, Steinberg F, Gallon M, Ghai R, Pim D, Langton P, Pearson N, Danson CM, Nägele H, Morris LL, Singla A, Overlee BL, Heesom KJ, Sessions R, Banks L, Collins BM, Berger I, Billadeau DD, Burstein E, Cullen PJ. 2017. Retriever is a multiprotein complex for retromer-independent endosomal cargo recycling. *Nat Cell Biol* **19**:1214–1225. doi:10.1038/ncb3610

Mecozzi VJ, Berman DE, Simoes S, Vetanovetz C, Awal MR, Patel VM, Schneider RT, Petsko GA, Ringe D, Small SA. 2014. Pharmacological chaperones stabilize retromer to limit APP processing. *Nat Chem Biol* **10**:443–449. doi:10.1038/nchembio.1508

Mehta SQ, Hiesinger PR, Beronja S, Zhai RG, Schulze KL, Verstreken P, Cao Y, Zhou Y, Tepass U, Crair MC, Bellen HJ. 2005. Mutations in Drosophila sec15 reveal a function in neuronal targeting for a subset of exocyst components. *Neuron* **46**:219–232. doi:10.1016/j.neuron.2005.02.029

Menzies FM, Fleming A, Rubinsztein DC. 2015. Compromised autophagy and neurodegenerative diseases. *Nat Rev Neurosci* **16**:345–357. doi:10.1038/nrn3961

Mitter D, Reisinger C, Hinz B, Hollmann S, Yelamanchili S V., Treiber-Held S, Ohm TG, Herrmann A, Ahnert-Hilger G. 2003. The synaptophysin/synaptobrevin interaction critically depends on the cholesterol content. *J Neurochem* **84**:35–42. doi:10.1046/j.1471-4159.2003.01258.x

Muhammad A, Flores I, Zhang H, Yu R, Staniszewski A, Planel E, Herman M, Ho L, Kreber R, Honig LS, Ganetzky B, Duff K, Arancio O, Small SA. 2008. Retromer deficiency observed in Alzheimer's disease causes hippocampal dysfunction, neurodegeneration, and Aβ accumulation. *Proc Natl Acad Sci U S A* **105**:7327–7332. doi:10.1073/pnas.0802545105

Munsie LN, Milnerwood AJ, Seibler P, Beccano-Kelly DA, Tatarnikov I, Khinda J, Volta M, Kadgien C, Cao LP, Tapia L, Klein C, Farrer MJ. 2015. Retromer-dependent neurotransmitter receptor trafficking to synapses is altered by the Parkinson's disease VPS35 mutation p.D620N. *Hum Mol Genet* **24**:1691–1703. doi:10.1093/hmg/ddu582

Nagarkar-Jaiswal S, Lee PT, Campbell ME, Chen K, Anguiano-Zarate S, Gutierrez MC, Busby T, Lin WW, He Y, Schulze KL, Booth BW, Evans-Holm M, Venken KJT, Levis RW, Spradling AC, Hoskins RA, Bellen HJ. 2015. A library of MiMICs allows tagging of genes and reversible, spatial and temporal knockdown of proteins in Drosophila. *Elife* **2015**. doi:10.7554/eLife.05338

Newsome TP, Åsling B, Dickson BJ. 2000. Analysis of Drosophila photoreceptor axon guidance in eye-specific mosaics. *Development* **127**:851–860.

Ohara S, Ukita Y, Ninomiya H, Ohno K. 2004. Axonal dystrophy of dorsal root ganglion sensory neurons in a mouse model of Niemann-Pick disease type C. *Exp Neurol* **187**:289–298. doi:10.1016/j.expneurol.2004.03.002

Ojelade SA, Lee T V., Giagtzoglou N, Yu L, Ugur B, Duraine L, Zuo Z, Petyuk V, De Jager PL, Bennett

DA, Arenkiel BR, Bellen HJ, Shulman J. 2019. Cindr, the Drosophila Homolog of the CD2AP Alzheimer's Disease Susceptibility Gene, is Required for Synaptic Transmission and Proteostasis. *SSRN Electron J* **28**:1799-1813.e5. doi:10.2139/ssrn.3312120

Piras A, Collin L, Grüninger F, Graff C, Rönnbäck A. 2016. Autophagic and lysosomal defects in human tauopathies: analysis of post-mortem brain from patients with familial Alzheimer disease, corticobasal degeneration and progressive supranuclear palsy. *Acta Neuropathol Commun* **4**:22. doi:10.1186/s40478-016-0292-9

Pocha SM, Wassmer T, Niehage C, Hoflack B, Knust E. 2011. Retromer controls epithelial cell polarity by trafficking the apical determinant crumbs. *Curr Biol* **21**:1111–1117. doi:10.1016/j.cub.2011.05.007

Reddy J V., Seaman MNJ. 2001. Vps26p, a component of retromer, directs the interactions of Vps35p in endosome-to-Golgi retrieval. *Mol Biol Cell* **12**:3242–3256. doi:10.1091/mbc.12.10.3242

Repnik U, Česen MH, Turk B. 2013. The endolysosomal system in cell death and survival. *Cold Spring Harb Perspect Biol* **5**. doi:10.1101/cshperspect.a008755

Rousseaux MWC, Vázquez-Vélez GE, Al-Ramahi I, Jeong HH, Bajić A, Revelli JP, Ye H, Phan ET, Deger JM, Perez AM, Kim JY, Lavery LA, Xu Q, Li MZ, Kang H, Kim JJ, Shulman JM, Westbrook TF, Elledge SJ, Liu Z, Botas J, Zoghbi HY. 2018. A druggable genome screen identifies modifiers of α-synuclein levels via a tiered cross-species validation approach. *J Neurosci* **38**:9286–9301. doi:10.1523/JNEUROSCI.0254-18.2018

Rui YN, Xu Z, Patel B, Chen Z, Chen D, Tito A, David G, Sun Y, Stimming EF, Bellen HJ, Cuervo AM, Zhang S. 2015. Huntingtin functions as a scaffold for selective macroautophagy. *Nat Cell Biol* **17**:262–275. doi:10.1038/ncb3101

Sambri I, D'Alessio R, Ezhova Y, Giuliano T, Sorrentino NC, Cacace V, De Risi M, Cataldi M, Annunziato L, De Leonibus E, Fraldi A. 2017. Lysosomal dysfunction disrupts presynaptic maintenance and restoration of presynaptic function prevents neurodegeneration in lysosomal storage diseases. *EMBO Mol Med* **9**:112–132. doi:10.15252/emmm.201606965

Seaman MNJ, Harbour ME, Tattersall D, Read E, Bright N. 2009. Membrane recruitment of the cargo-selective retromer subcomplex is catalysed by the small GTPase Rab7 and inhibited by the Rab-GAP TBC1D5. *J Cell Sci* **122**:2371–2382. doi:10.1242/jcs.048686

Seaman MNJ, Marcusson EG, Cereghino JL, Emr SD. 1997. Endosome to Golgi retrieval of the vacuolar protein sorting receptor, Vps10p, requires the function of the VPS29, VPS30, and VPS35 gene products. *J Cell Biol* **137**:79–92. doi:10.1083/jcb.137.1.79

Seaman MNJ, McCaffery JM, Emr SD. 1998. A membrane coat complex essential for endosome-to-Golgi retrograde transport in yeast. *J Cell Biol* **142**:665–681. doi:10.1083/jcb.142.3.665

Small SA, Petsko GA. 2015. Retromer in Alzheimer disease, Parkinson disease and other neurological disorders. *Nat Rev Neurosci* **16**:126–132. doi:10.1038/nrn3896

Soukup S, Vanhauwaert R, Verstreken P. 2018. Parkinson's disease: convergence on synaptic homeostasis. *EMBO J* **37**. doi:10.15252/embj.201898960

Starble R, Pokrywka NJ. 2018. The retromer subunit Vps26 mediates Notch signaling during Drosophila oogenesis. *Mech Dev* **149**:1–8. doi:10.1016/j.mod.2017.10.001

Stokin GB, Lillo C, Falzone TL, Brusch RG, Rockenstein E, Mount SL, Raman R, Davies P, Masliah E, Williams DS, Goldstein LSB. 2005. Axonopathy and transport deficits early in the pathogenesis of Alzheimer's diseases. *Science (80-)* **307**:1282–1288. doi:10.1126/science.1105681

Strutt H, Langton PF, Pearson N, McMillan KJ, Strutt D, Cullen PJ. 2019. Retromer Controls Planar Polarity Protein Levels and Asymmetric Localization at Intercellular Junctions. *Curr Biol* **29**:484-491.e6. doi:10.1016/j.cub.2018.12.027

Tang FL, Erion JR, Tian Y, Liu W, Yin DM, Ye J, Tang B, Mei L, Xiong WC. 2015a. VPS35 in dopamine neurons is required for endosome-to- golgi retrieval of Lamp2a, a receptor of chaperone-mediated autophagy that is critical for α-synuclein degradation and prevention of pathogenesis of Parkinson's disease. *J Neurosci* **35**:10613–10628. doi:10.1523/JNEUROSCI.0042-15.2015

Tang FL, Liu W, Hu JX, Erion JR, Ye J, Mei L, Xiong WC. 2015b. VPS35 Deficiency or Mutation Causes Dopaminergic Neuronal Loss by Impairing Mitochondrial Fusion and Function. *Cell Rep*

12:1631–1643. doi:10.1016/j.celrep.2015.08.001

Temkin P, Morishita W, Goswami D, Arendt K, Chen L, Malenka R. 2017. The Retromer Supports AMPA Receptor Trafficking During LTP. *Neuron* **94**:74-82.e5. doi:10.1016/j.neuron.2017.03.020

Tian Y, Tang FL, Sun XD, Wen L, Mei L, Tang BS, Xiong WC. 2015. VPS35-deficiency results in an impaired AMPA receptor trafficking and decreased dendritic spine maturation. *Mol Brain* **8**:70. doi:10.1186/s13041-015-0156-4

Tsika E, Glauser L, Moser R, Fiser A, Daniel G, Sheerin UM, Lees A, Troncoso JC, Lewis PA, Bandopadhyay R, Schneider BL, Moore DJ. 2014. Parkinson's disease-linked mutations in VPS35 induce dopaminergic neurodegeneration. *Hum Mol Genet* **23**:4621–4638. doi:10.1093/hmg/ddu178

Uytterhoeven V, Kuenen S, Kasprowicz J, Miskiewicz K, Verstreken P. 2011. Loss of Skywalker reveals synaptic endosomes as sorting stations for synaptic vesicle proteins. *Cell* **145**:117–132. doi:10.1016/j.cell.2011.02.039

Vagnozzi AN, Li JG, Chiu J, Razmpour R, Warfield R, Ramirez SH, Praticò D. 2019. VPS35 regulates tau phosphorylation and neuropathology in tauopathy. *Mol Psychiatry*. doi:10.1038/s41380-019-0453-x

Vazquez-Sanchez S, Bobeldijk S, Dekker MP, Van Keimpema L, Van Weering JRT. 2018. VPS35 depletion does not impair presynaptic structure and function. *Sci Rep* **8**. doi:10.1038/s41598-018-20448-4

Venken KJT, Carlson JW, Schulze KL, Pan H, He Y, Spokony R, Wan KH, Koriabine M, de Jong PJ, White KP, Bellen HJ, Hoskins RA. 2009. Versatile P[acman] BAC libraries for transgenesis studies in Drosophila melanogaster. *Nat Methods* **6**:431–434. doi:10.1038/nmeth.1331

Verstreken P, Kjaerulff O, Lloyd TE, Atkinson R, Zhou Y, Meinertzhagen IA, Bellen HJ. 2002. Endophilin mutations block clathrin-mediated endocytosis but not neurotransmitter release. *Cell* **109**:101–112. doi:10.1016/S0092-8674(02)00688-8

Verstreken P, Ohyama T, Bellen HJ. 2008. FM 1-43 labeling of synaptic vesicle pools at the drosophila neuromuscular junction. *Methods Mol Biol* **440**:349–369. doi:10.1007/978-1-59745-178-9_26

Vilariño-Güell C, Wider C, Ross OA, Dachsel JC, Kachergus JM, Lincoln SJ, Soto-Ortolaza AI, Cobb SA, Wilhoite GJ, Bacon JA, Bahareh Behrouz, Melrose HL, Hentati E, Puschmann A, Evans DM, Conibear E, Wasserman WW, Aasly JO, Burkhard PR, Djaldetti R, Ghika J, Hentati F, Krygowska-Wajs A, Lynch T, Melamed E, Rajput A, Rajput AH, Solida A, Wu RM, Uitti RJ, Wszolek ZK, Vingerhoets F, Farrer MJ. 2011. VPS35 mutations in parkinson disease. *Am J Hum Genet* **89**:162–167. doi:10.1016/j.ajhg.2011.06.001

Walsh RB, Becalska AN, Zunitch MJ, Wang S, Isaac B, Yeh A, Koles K, Rodal AA. 2019. Opposing functions for retromer and Rab11 in extracellular vesicle cargo traffic at synapses. *bioRxiv* 645713. doi:10.1101/645713

Wang S, Bellen HJ. 2015. The retromer complex in development and disease. *Dev* **142**:2392–2396. doi:10.1242/dev.123737

Wang S, Tan KL, Agosto MA, Xiong B, Yamamoto S, Sandoval H, Jaiswal M, Bayat V, Zhang K, Charng WL, David G, Duraine L, Venkatachalam K, Wensel TG, Bellen HJ. 2014. The Retromer Complex Is Required for Rhodopsin Recycling and Its Loss Leads to Photoreceptor Degeneration. *PLoS Biol* **12**:e1001847. doi:10.1371/journal.pbio.1001847

Wang YC, Lauwers E, Verstreken P. 2017. Presynaptic protein homeostasis and neuronal function. *Curr Opin Genet Dev* **44**:38–46. doi:10.1016/j.gde.2017.01.015

Wen L, Tang FL, Hong Y, Luo SW, Wang CL, He W, Shen C, Jung JU, Xiong F, Lee D hoon, Zhang QG, Brann D, Kim TW, Yan R, Mei L, Xiong WC. 2011. VPS35 haploinsufficiency increases Alzheimer's disease neuropathology. *J Cell Biol* **195**:765–779. doi:10.1083/jcb.201105109

Winther ÅME, Jiao W, Vorontsova O, Rees KA, Koh TW, Sopova E, Schulze KL, Bellen HJ, Shupliakov O. 2013. The dynamin-binding domains of Dap160/intersectin affect bulk membrane retrieval in synapses. *J Cell Sci* **126**:1021–1031. doi:10.1242/jcs.118968

Wu S, Fagan RR, Uttamapinant C, Lifshitz LM, Fogarty KE, Ting AY, Melikian HE. 2017. The dopamine transporter recycles via a retromer-dependent postendocytic mechanism: Tracking studies using a novel fluorophore-coupling approach. *J Neurosci* **37**:9438–9452.

doi:10.1523/JNEUROSCI.3885-16.2017

Young JE, Fong LK, Frankowski H, Petsko GA, Small SA, Goldstein LSB. 2018. Stabilizing the Retromer Complex in a Human Stem Cell Model of Alzheimer's Disease Reduces TAU Phosphorylation Independently of Amyloid Precursor Protein. *Stem Cell Reports* **10**:1046–1058. doi:10.1016/j.stemcr.2018.01.031

Ysselstein D, Shulman JM, Krainc D. 2019. Emerging links between pediatric lysosomal storage diseases and adult parkinsonism. *Mov Disord* **34**:614–624. doi:10.1002/mds.27631

Zavodszky E, Seaman MNJ, Moreau K, Jimenez-Sanchez M, Breusegem SY, Harbour ME, Rubinsztein DC. 2014. Mutation in VPS35 associated with Parkinson's disease impairs WASH complex association and inhibits autophagy. *Nat Commun* **5**. doi:10.1038/ncomms4828

Zimprich A, Benet-Pagès A, Struhal W, Graf E, Eck SH, Offman MN, Haubenberger D, Spielberger S, Schulte EC, Lichtner P, Rossle SC, Klopp N, Wolf E, Seppi K, Pirker W, Presslauer S, Mollenhauer B, Katzenschlager R, Foki T, Hotzy C, Reinthaler E, Harutyunyan A, Kralovics R, Peters A, Zimprich F, Brücke T, Poewe W, Auff E, Trenkwalder C, Rost B, Ransmayr G, Winkelmann J, Meitinger T, Strom TM. 2011. A mutation in VPS35, encoding a subunit of the retromer complex, causes late-onset parkinson disease. *Am J Hum Genet* **89**:168–175. doi:10.1016/j.ajhg.2011.06.008

Funding

This study was supported by grants from the NIH (R01AG053960, R01NS103967, U01AG046161, U01AG061357). J.M.S. was additionally supported by Huffington Foundation, Jan and Dan Duncan Neurological Research Institute at Texas Children's Hospital, and a Career Award for Medical Scientists from the Burroughs Wellcome Fund. S.A.O. was supported by a Postdoctoral Enrichment Program Award from the Burroughs Wellcome Fund (BWF-1017399) and an Alzheimer's Association fellowship (AARFD-16-442630). D.L.-K. was supported by the Belfer Foundation. H.J.B. is an Investigator with the Howard Hughes Medical Institute. The Pathology and Histology Core at Baylor

College of Medicine is supported by NIH grant P30CA125123. The work was additionally supported by U54HD083092 from the Eunice Kennedy Shriver National Institute of Child Health & Human Development; the IDDRC Microscopy Core was used for this project.

Acknowledgements

We thank Drs. L. Partridge, S. Zhang, and P.R. Hiesinger for providing antibodies and *Drosophila* stocks. We also thank the Bloomington *Drosophila* Stock Center, the Vienna *Drosophila* RNAi Center, the Developmental Studies Hybridoma Bank, and FlyBase (Gramates et al., 2017). We thank Y. He and L. Duraine for research technical support. We are grateful to Drs. M. Sardiello, K. Venkatachalam, J. Botas, and H. Zoghbi for feedback and discussions.

Author Contributions

Conceptualization, H.Y., J.M.S.; Investigation, H.Y., S.O., D.L.-K., Z.Z., L.W., Y.L.; Analysis/Interpretation, H.Y., S.O., H.J.B., J.M.S.; Writing—Original Draft, H.Y., J.M.S.; Writing—Review & Editing, H.Y., S.O., Z.Z., D.L.-K., L.W., Y.L., U.T., A.A.R., H.J.B., J.M.S.; Reagents, J.Y.J.G., U.T., A.A.R.; Funding Acquisition, A.A.R., H.J.B., J.M.S.; Supervision, H.J.B., J.M.S.

Competing Interests

The authors declare no competing interests

Figures and Legends

Figures 1-8 and Figures S1-S6 follow, along with legends.

Figure 1

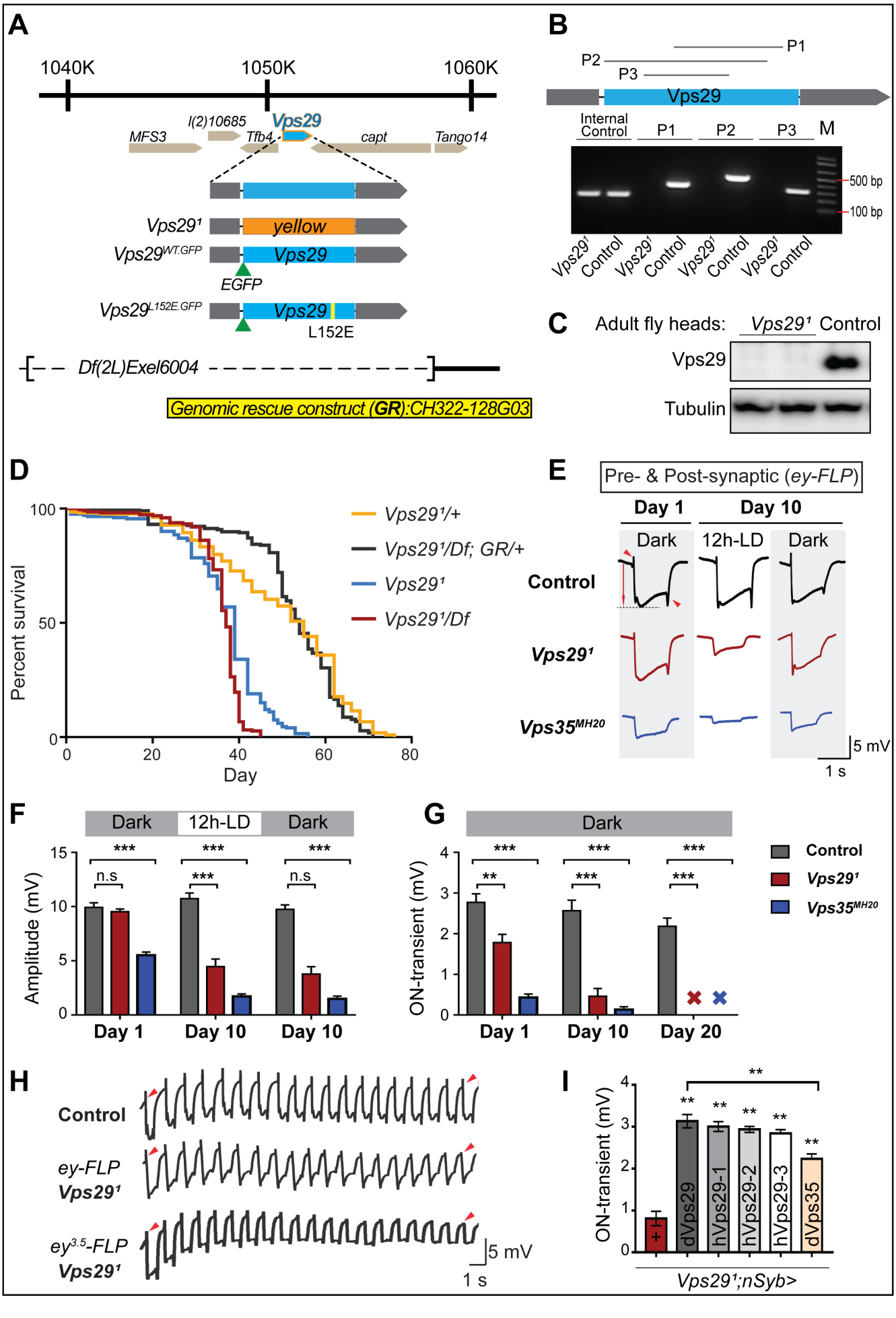

Figure 1: *Vps29* is required for age-dependent retinal function

(**A**) The *Vps29* genomic locus is shown, highlighting reagents used in this study. In the null allele, $Vps29^{1}$, the gene coding sequence (blue) is replaced by a $ywing^{2+}$ marker gene. $Vps29^{WT.GFP}$ and $Vps29^{L152E.GFP}$ are identical N-terminal tagged-Vps29 alleles, except for the L152E variant. A chromosomal deficiency *Df(2L)Exel6004* is shown, with the deleted regions indicated by dashed lines. A bacterial artificial chromosome (BAC) (yellow) was used for transgenic genomic rescue (*GR*). (**B**) Genomic polymerase chain reaction (PCR) showing loss of Vps29 coding sequence in $Vps29^{1}$ homozygotes versus control (*w*) flies. P1, P2, and P3 denote expected PCR products from primer pairs targeting *Vps29* genomic sequence. As an additional control, PCR was also performed for *Vps35* genomic sequence. (**C**) Western blot from adult heads probed with anti-Vps29 antibody, confirming $Vps29^{1}$ is a protein null allele. (**D**) $Vps29^{1}$ homozygotes and $Vps29^{1}/Df$ transheterozygotes ($Vps29^{1}/Df(2L)Exel6004$) show reduced survival that is rescued by the *Vps29* genomic rescue strain ($Vps29^{1}/Df;\ GR/+$). Quantitation based on n = 200-235 per group. See also **Figure S1A**. (**E**) Representative ERG traces at 1- and 10-days after generation of *ey-FLP* clones from (i) control (*FRT40A*), (ii) $Vps29^{1}$, or (iii) $Vps35^{MH20}$. Flies were raised using an alternating 12-hour light/dark cycle (12h-LD) or in complete darkness. Loss of either *Vps29* or *Vps35* disrupted light-induced depolarization (arrow) in 10-day-old flies. On- & off- transient ERG potentials (top and bottom arrowheads, respectively) were also lost. Raising flies in the dark restored ERG depolarization, but not the transients, indicating persistent defects in synaptic transmission. (**F-G**) Quantification (n=6-8) of ERG depolarization and on-transient potentials. See also **Figure S1B**. (**H**) Compared with controls (*FRT40A* clones), ERG transient potentials are extinguished by rapid stimulation in $Vps29^{1}$ clones. Consistent results were obtained using either *ey-FLP* or $ey^{3.5}$*-FLP*, which targets presynaptic neurons only. Flies were raised in complete darkness and examined at 1-day. See also **Figure S1C**. (**I**) Rescue of $Vps29^{1}$ synaptic transmission defects by pan-neuronal expression (*nSyb-GAL4* driver) of either *Drosophila Vps29* or *Vps35* (*dVps29* and *dVps35*) or human *Vps29* (*hVps29-1,-2,* or *-3*, representing 3 alternate isoforms). Quantification of ERG on-transients in 15-day-old flies (n=9-12 per group) from the following genotypes:
(1) $Vps29^{1}$*;nSyb-Gal4/+*; (2) $Vps29^{1}$*;nSyb-Gal4/UAS-dVps29*; (3-5) $Vps29^{1}$*;nSyb-Gal4/UAS-hVps29*; and
(6) $Vps29^{1}$*;nSyb-Gal4/UAS-dVps35*. Statistical analysis (**F, G, I**) based on one-way ANOVA. All error bars denote SEM. n.s. not significant; ** $p<0.01$; *** $p<0.001$.

Figure 2

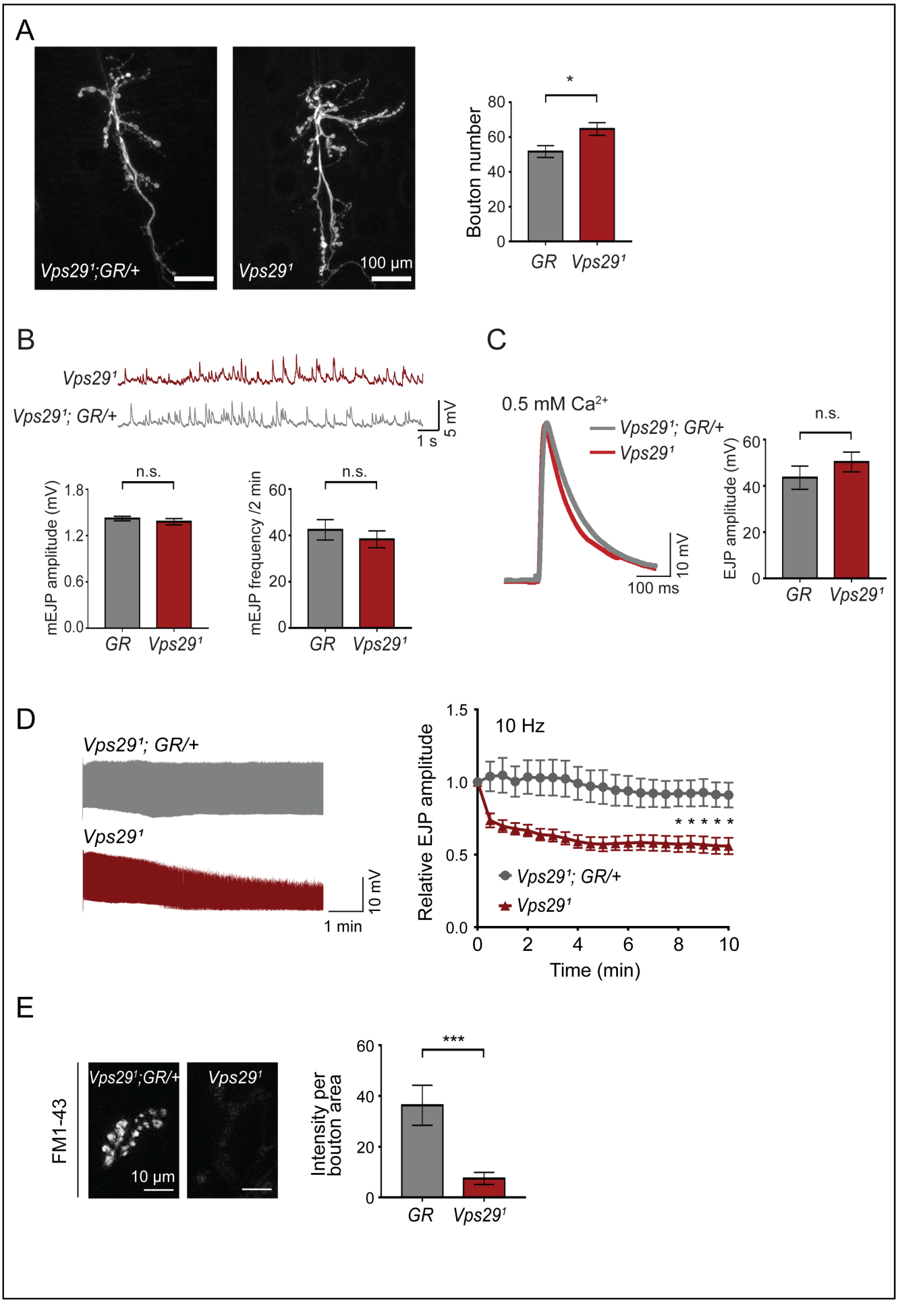

Figure 2: Retromer regulates synaptic vesicle endocytosis and recycling

(**A**) *Vps29* loss of function causes an increased number of synaptic terminal boutons at the larval neuromuscular junction (NMJ). NMJ preparations from *Vps29^{1}* homozygotes or control larvae (*GR = Vps29^{1};GR/+*) were stained with an antibody against horseradish peroxidase, and Type IIb boutons at abdominal segments A2 and A3 were quantified (n=5 animals per group). The *Vps29* transgenic BAC (GR) was heterozygous for all comparisons. (**B**) Larval NMJ electrophysiology in *Vps29^{1}* reveals normal miniature excitatory junction potential (mEJP) amplitude and frequency (in 2 min) (n=14-16). (**C**) Evoked excitatory junction potentials (EJPs) are normal in the absence of *Vps29*. Representative EJP traces from *Vps29^{1}* and *Vps29^{1};GR/+* (control, *GR*) larvae and quantification (n=13-15). 0.2 Hz stimulation was performed using 0.5 mM Ca^{2+}. (**D**) *Vps29^{1}* NMJs show synaptic depression following rapid stimulation (10 Hz, 0.5 mM extracellular Ca^{2+}). Representative traces (10 min) are shown, with quantification (n=13). Data was normalized to initial EJP amplitude. (**E**) *Vps29^{1}* NMJs show reduced FM1-43 dye uptake following KCl stimulation, consistent with impaired synaptic vesicle endocytosis. FM1-43 signal intensity (per bouton area) was quantified (n=8-11). See also **Figure S1D**. Statistical analysis (**A-E**) based on Student's t-test. All error bars denote SEM. n.s. not significant; * $p<0.05$; *** $p<0.001$.

Figure 3

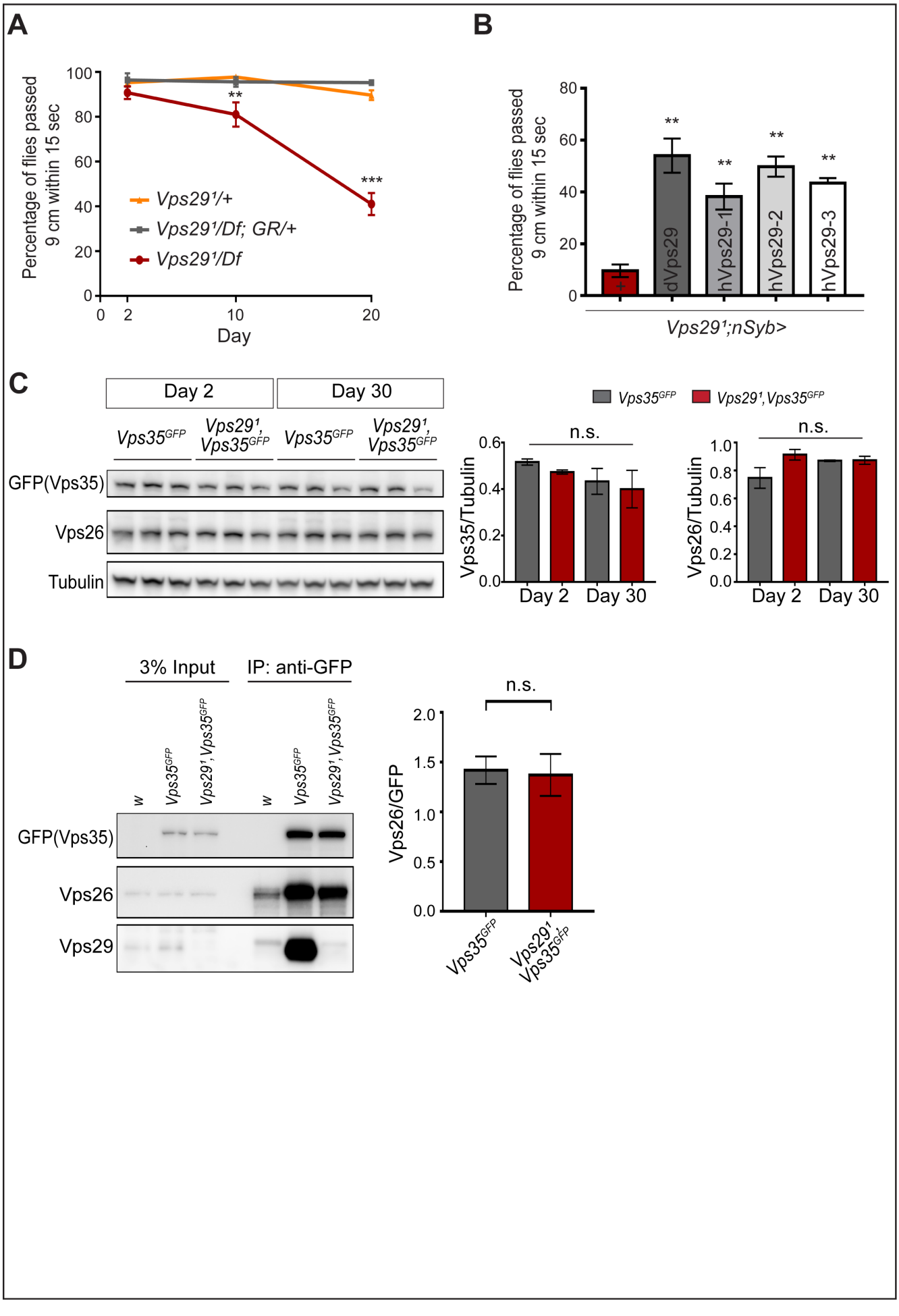

Figure 3: Progressive locomotor impairment in *Vps29* mutants but preserved Vps35 and Vps26 proteins.

(**A**) *Vps29^{1}/Df* adults demonstrate age-dependent locomotor impairment, based on startle-induced negative geotaxis, and this phenotype is fully rescued by a single, heterozygous copy of the *Vps29* BAC transgenic (*Vps29^{1}/Df; GR/+*). Quantification based on n=4 groups, each consisting 13-16 flies. See also **Figure S2A**. (**B**) Pan-neuronal expression of either *Drosophila* or human *Vps29* (dVps29 or hVps29, respectively), using the *nsyb-GAL4* driver rescues the *Vps29^{1}* locomotor phenotype. Quantification based on n=4 groups of 20-day-old flies from the following genotypes: (1) *Vps29^{1};nSyb-Gal4/+*; (2) *Vps29^{1};nSyb-Gal4/UAS-dVps29*; and (3-5) *Vps29^{1};nSyb-Gal4/UAS-hVps29*. (**C**) Vps35 and Vps26 protein levels are normal in the absence of *Vps29*. Western blots of adult fly head homogenates from either *Vps29^{1}, Vps35^{GFP}* homozygotes or controls (*Vps35^{GFP}*), probed for Vps35^{GFP} (anti-GFP), Vps26, or Tubulin (loading control). Quantification based on n=3 replicate experiments. See also **Figure S2B & C**. (**D**) The association of Vps35 and Vps26 proteins is preserved in the absence of *Vps29*. Vps35^{GFP} was immunoprecipitated from either *Vps29^{1}, Vps35^{GFP}* homozygotes or control animals (*Vps35^{GFP}*) (2-day old), and western blots were probed for Vps35^{GFP} (anti-GFP), Vps26, and Vps29. Quantification based on n=4 replicate experiments. Statistical analysis based on one-way ANOVA (**A-C**) or Student's t- test (**D**). All error bars denote SEM. n.s. not significant; ** $p<0.01$; *** $p<0.001$.

Figure 4

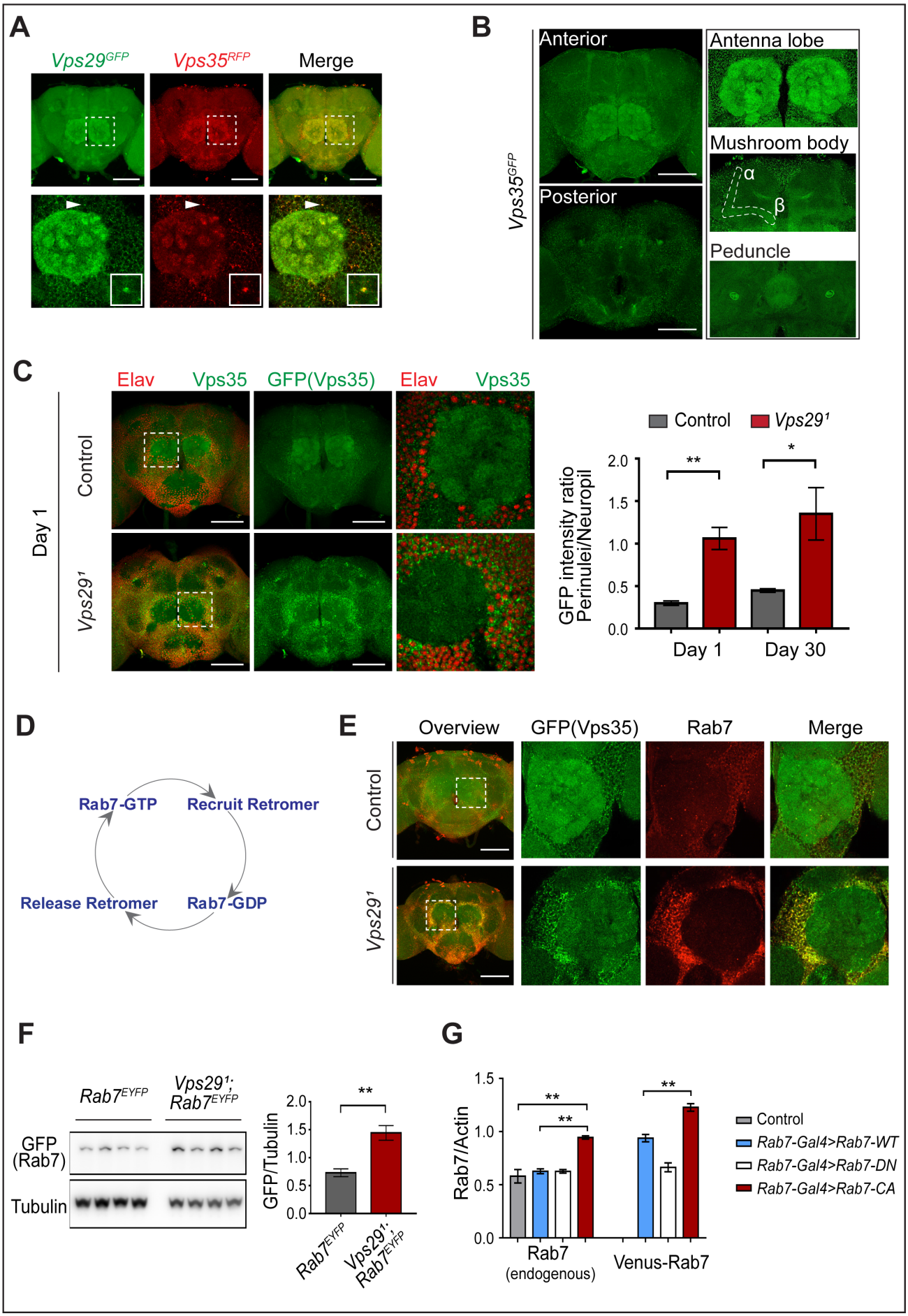

Figure 4: *Vps29* regulates Vps35 localization in the adult brain.

(**A**) $Vps29^{GFP}$ (anti-GFP, green) and $Vps35^{RFP}$ (red) are expressed throughout the adult brain and co-localize. Boxed region of interest including antennal lobe (top row) is shown magnified (bottom row). Representative puncta (arrowhead) co-staining for Vps35 and Vps29 is further magnified in inset. Scale bars, 100 µm. **(B**) $Vps35^{GFP}$ (anti-GFP, green) is modestly enriched in neuropil regions, including the antennal lobes and the mushroom body (α-/β- lobes and peduncles). Scale bars, 100 µm. See also **Figure S3A**. (**C**) In the absence of *Vps29*, $Vps35^{GFP}$ (green) protein is redistributed in the adult brain, shifting from neuropil to soma and forming large perinuclear puncta. Neuronal nuclei are labeled with anti-Elav (red). Within the boxed region of interest, including antennal lobe and surrounding nuclei, the GFP intensity ratio (perinuclear to neuropil) was quantified (n=3) in $Vps29^{1}$, $Vps35^{GFP}$ homozygotes or $Vps35^{GFP}$ controls. Scale bars, 100 µm. (**D**) Schematic highlighting the Rab7 cycle including GTP-bound (active) and GDP-bound (inactive) forms and putative interactions regulating retromer recruitment and release. (**E**) In *Vps29* mutants, $Vps35^{GFP}$ (green) colocalizes with Rab7 (anti-Rab7, red), which appears increased and similarly redistributed from neuropil to soma. Boxed region of interest is shown magnified at right. Scale bars, 100 µm. See also **Figure S3B**. (**F**) Rab7 protein levels are increased in the absence of *Vps29*. Western blots of adult head homogenates, including $Vps29^{1}$, $Rab7^{EYFP}$ homozygotes or $Rab7^{EYFP}$ controls (2-day-old), were probed for Rab7-YFP (anti-GFP) and Tubulin (loading control). Quantification based on n=4 replicate experiments. See also **Figure S3B, C**. (**G**) Rab7 protein levels are increased in the constitutive active, "GTP-locked" $Rab7^{Q67L}$ mutant. Western blots of adult head homogenates from 5-day old animals were probed for Rab7 or Actin, including the following genotypes: (1, *Rab7-Gal4>Rab7-CA*) *UAS-Venus-Rab7*^{Q67L}*/+; Rab7-Gal4/+*; (2, *Rab7-Gal4>Rab7-WT*) *UAS-Venus-Rab7*^{WT}*/+; Rab7-Gal4/+*; (3, *Rab7-Gal4>Rab7-DN*) *UAS-Venus-Rab7*^{T22N}*/+; Rab7-Gal4/+*; (4, control) *w*. Venus-tagged or endogenous Rab7 protein levels were separately quantified, based on n=4 replicate experiments. See also **Figure S3D**. Statistical analysis was based on Student's t-test (**C, F**) or one-way ANOVA (**G**). All error bars denote SEM. * $p<0.05$; ** $p<0.01$.

Figure 5

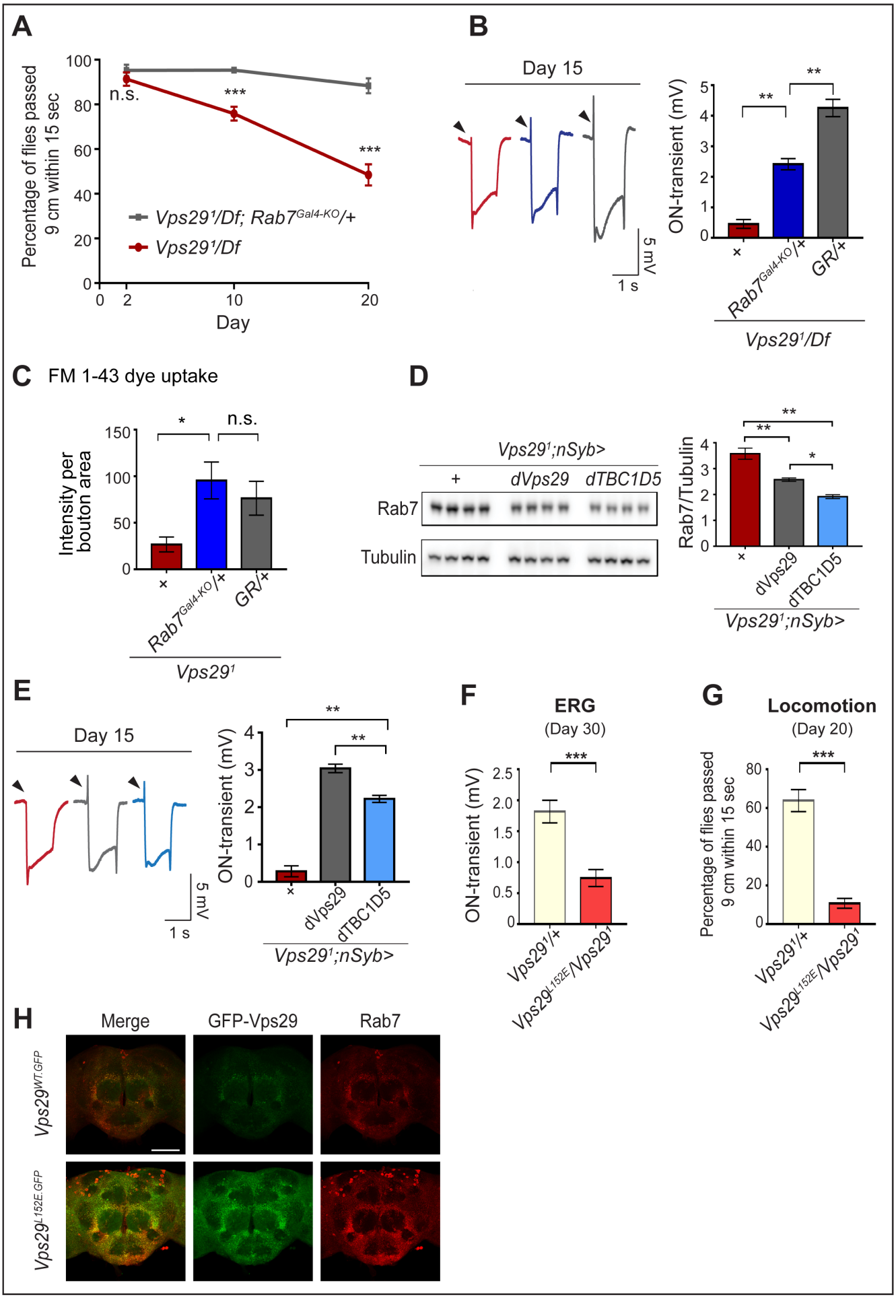

Figure 5: Reduction of Rab7 or overexpression of TBC1D5 suppresses *Vps29* mutant phenotypes.

(**A-C**) Reduction of *Rab7* rescues *Vps29* mutant phenotypes, including progressive locomotor impairment (**A**), synaptic transmission (**B**), and synaptic vesicle endocytosis at the larval NMJ (**C**). (**A**) Quantification of locomotor behavior based on n=4 groups, each consisting of 12-15 flies. (**B**) Quantification of electroretinogram (ERG) on-transients (n=12-13) from adults raised using a 12h light/dark cycle. **(C)** FM1-43 dye uptake signal intensity per NMJ bouton area was quantified (n=7-9). (**D**) Pan-neuronal overexpression of *dTBC1D5* (*nsyb>dTBC1D5*) restores Rab7 protein level in flies lacking *Vps29*. Western blots of adult fly head homogenates (30-day-old) were probed for Rab7 and Tubulin (loading control), and quantified based on n=4 replicate experiments, including the following genotypes: (1, red) $Vps29^{1}$*;nSyb-GAL4/+*; (2, grey) $Vps29^{1}$*;nSyb-GAL4/UAS-dVps29*; (3, blue) $Vps29^{1}$*;nSyb-GAL4/UAS-dTBC1D5*. (**E**) Pan-neuronal overexpression of *dTBC1D5* (*nsyb>dTBC1D5*) rescues synaptic transmission in $Vps29^{1}$ mutants. Quantification of ERG on-transients (n=8) from adults raised using a 12h light/dark cycle. (**F, G**) The $Vps29^{L152E}$ mutation, predicted to disrupt the Vps29-TBC1D5 interaction, fails to complement $Vps29^{1}$, causing impaired synaptic transmission (**F**) and locomotor impairment (**G**). Quantification of ERG on-transients (**F**, n=12-14) or locomotor behavior (**G**, n=5-6 groups). See also **Figure S4A**. **(H**) The $Vps29^{L152E}$ mutation causes increased expression of Vps29 (anti-GFP, green) and Rab7 (anti-Rab7, red) and Vps29. Whole-mount brain immunofluorescence shown for $Vps29^{L152E.GFP}$ or $Vps29^{WT.GFP}$ homozygotes (2-day old adults). Scale bars, 100 µm. See also **Figure S4B**. Statistical analysis based on Student's t-test (**A, F, G**) or one-way ANOVA (**B-E**). All error bars denote SEM. n.s. not significant; * $p<0.05$; ** $p<0.01$; *** $p<0.001$

Figure 6

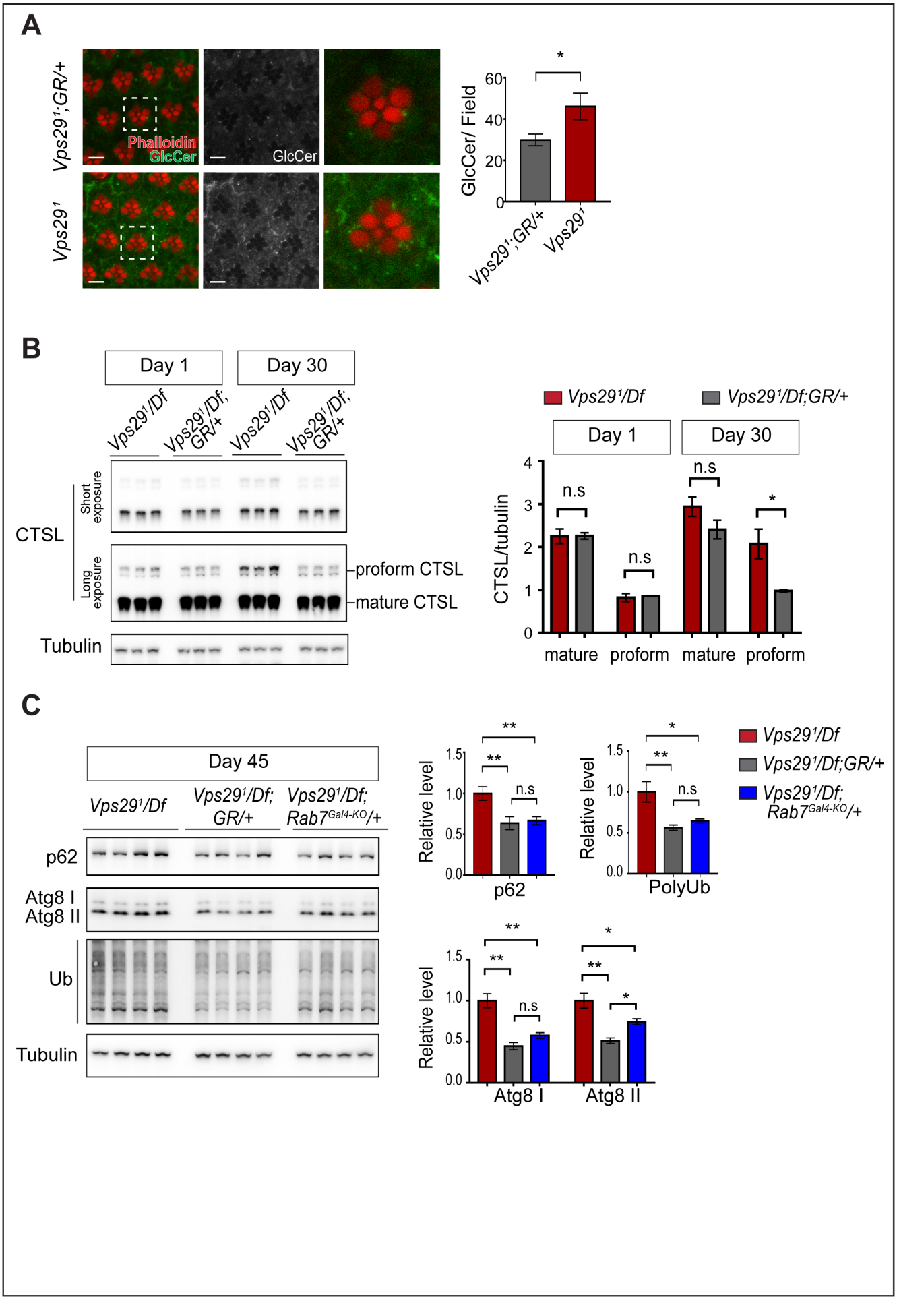

Figure 6: Loss of *Vps29* causes age-dependent, progressive lysosomal dysfunction in the brain.

(**A**) In the absence of *Vps29*, glucosylceramide (anti-GlcCer, green) accumulates in the retina. Tissue is counterstained for actin (phalloidin, red) to highlight the photoreceptor rhabdomeres. Glucosylceramide signal was quantified (n=10) in 30-day-old animals raised in dark conditions, including *GMR-w-RNAi/+; Vps29^{1}; GR/+* (controls) and *GMR-w-RNAi/+; Vps29^{1}*. Eye pigment was removed using RNAi against the *w* gene to reduce auto-fluorescence. Scale bars, 5 µm. (**B**) The uncleaved, CTSL proform is increased in aged animals lacking *Vps29*, consistent with diminished lysosomal proteolytic capacity. Western blots from adult fly head homogenates were probed for CTSL and Tubulin (loading control), and quantified based on n=3 replicate experiments. See also **Figure S5A**. (**C**) Autophagic flux is reduced in aged animals lacking *Vps29*, and this phenotype is suppressed by reduction of *Rab7*. Western blots of adult head homogenates were probed for autophagic markers, including p62, Atg8, polyubiquitin (FK1), or Tubulin (loading control), and quantified based on n=8 replicate experiments. See also **Figure S5B**, **C**. Statistical analysis based on Student's t-test (**A**, **B**) and one-way ANOVA (**C**). All error bars denote SEM. n.s. not significant; * $p<0.05$; ** $p<0.01$.

Figure 7

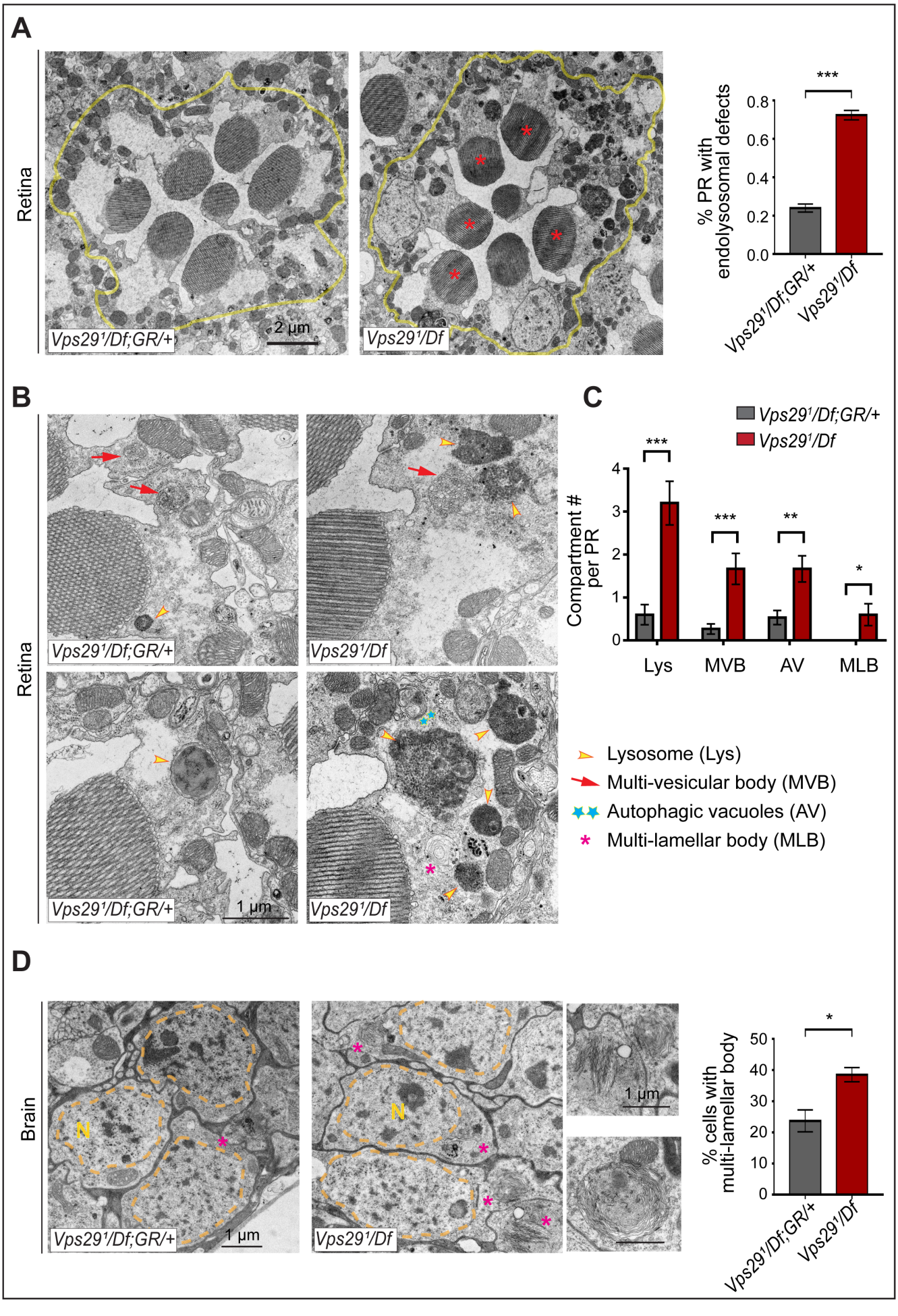

Figure 7: Loss of *Vps29* disrupts lysosomal ultrastructure in the brain.

(**A**) Transmission electron microscopy (TEM) reveals overall preserved photoreceptor morphology, but aberrant endolysosomal structures in retinae from 30-day-old animals lacking *Vps29*. Within each ommatidium (yellow outline), the percentage of photoreceptors (PR) with endolysosomal defects was quantified. Asterisks denote photoreceptors with aberrant endolysosomal structures. Quantification based on n=30 ommatidia from 3 animals per genotype. See also **Figure S6A**, **B**. (**B**) At higher magnification, TEM reveals an increase in lysosomes, multivesicular bodies, autophagic vacuoles, and multilamellar bodies in *Vps29* mutant retinae. Lysosomes were frequently observed to be aberrantly enlarged and filled with granular, electrodense material. (**C**) Distinct endolysosomal structures and/or compartments were quantified in n=15 photoreceptors, including 5 photoreceptors from 3 animals for each genotype. (**D**) Increased numbers of multi-lamellar bodies (asterisks) are observed in cortical neurons from brains 30-day-old animals lacking *Vps29*. Neuronal nuclei ("N") are outlined. Quantification based on cell counts from n=4 animals (50 cells per brain). See also **Figure S6D**. Statistical analysis (**A**, **C**, **D**) based on Student's t-test. All error bars denote SEM. * $p<0.05$; ** $p<0.01$; *** $p<0.001$.

Figure 8

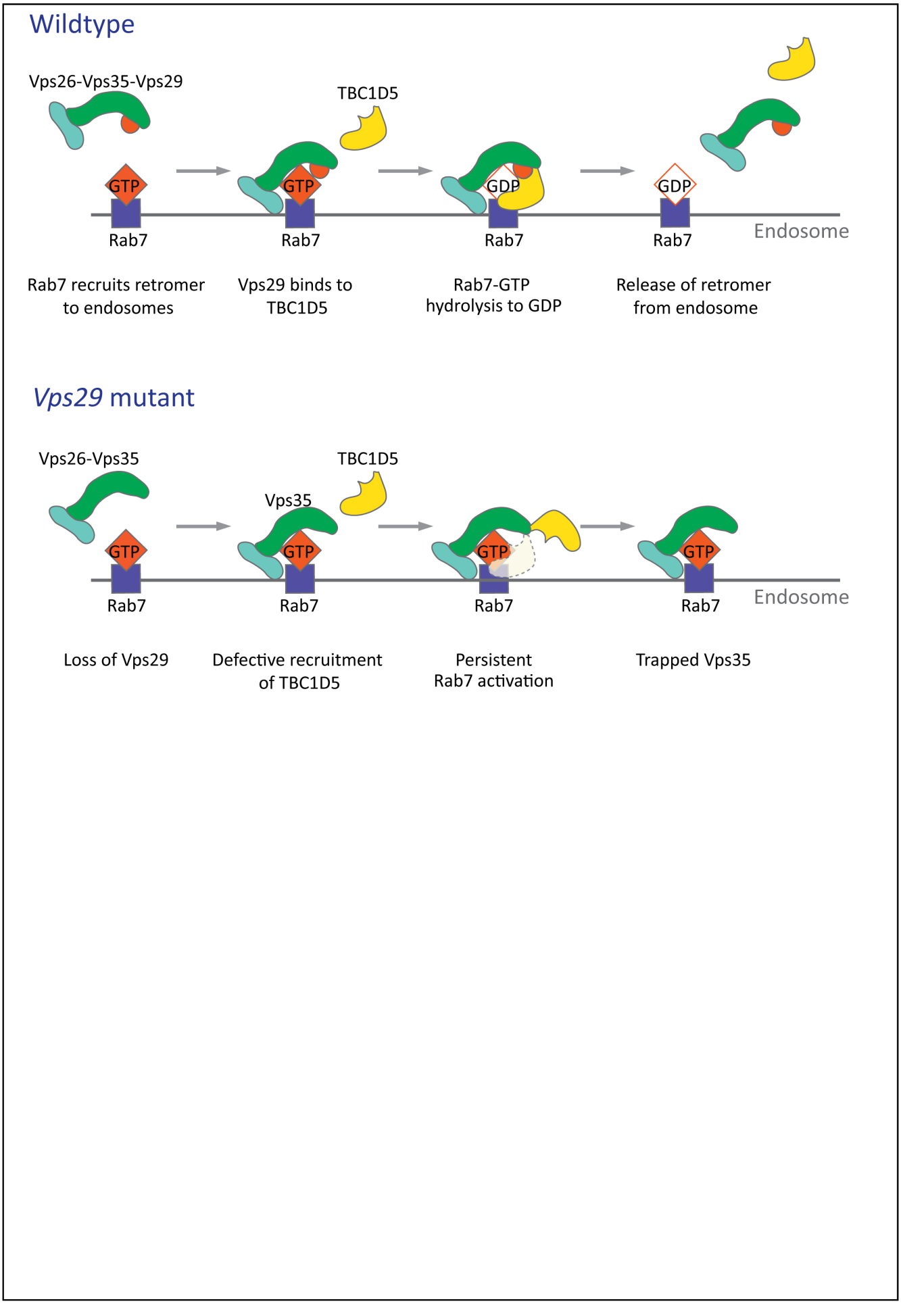

Figure 8: Model for Vps29-dependent Retromer Recruitment and Release.

In neurons, the retromer core Vp26-Vps35-Vps29 is recruited by Rab7 to the endosomal membrane. Vps29 engages TBC1D5, which promotes inactivation of Rab7 and release of Vps35. In the absence of *Vps29*, the residual retromer complex is trapped at the endosomal membrane.

Figure S1

A

Cross	Number	CyO	non-CyO	p-Value
Df(2L)Exel6004/CyO X *Vps29¹/CyO*	Observed	347	116	0.0002
	Expected	309	154	
Vps29¹/CyO X *Vps29¹/CyO*	Observed	234	74	0.0007
	Expected	206	102	

B

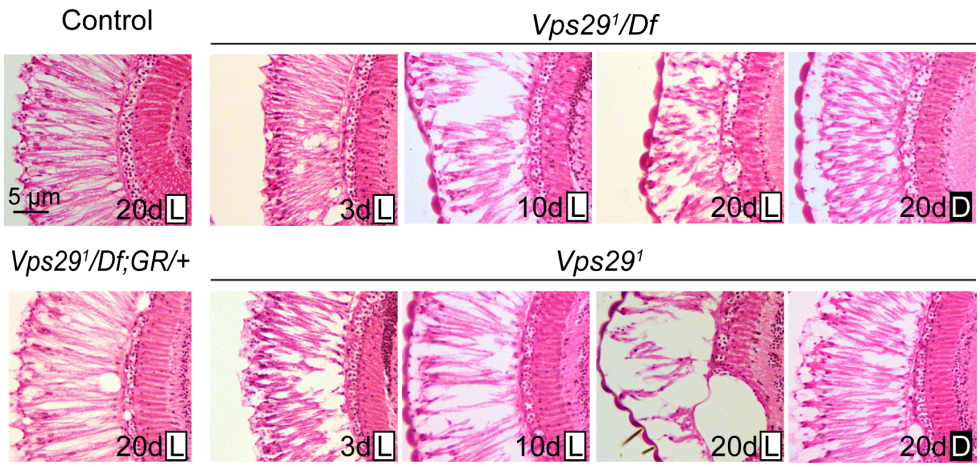

C

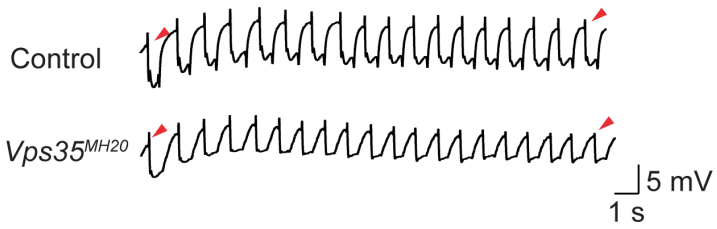

D

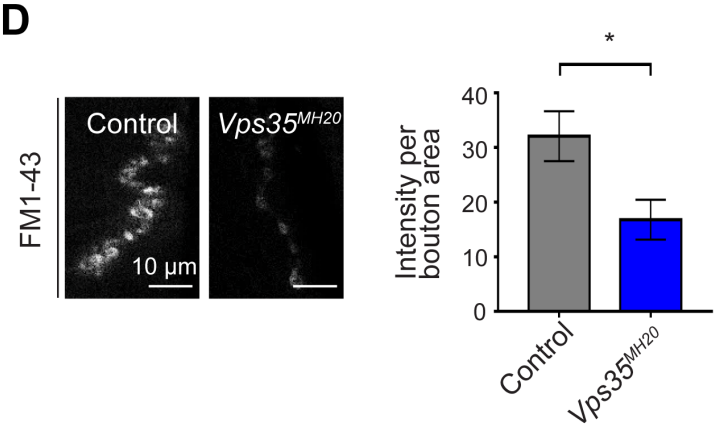

Figure S1 (Related to Figures 1 & 2): Additional studies of adult retina and neuromuscular junction.

(A) Adult flies lacking *Vps29* (*Vps29^{1}* homozygotes and *Vps29^{1}/Df*) are recovered at ratios below Mendelian expectations (~25% vs. 33%). For statistical analysis, a chi-square test was performed. **(B)** Loss of *Vps29* causes light- and age-dependent retinal degeneration. Frontal sections through the retina are shown, stained with hematoxylin & eosin, revealing vacuolar changes, which was suppressed by either introducing the *Vps29* genomic rescue construct (GR) or raising animals in dark conditions. *GMR-w-RNAi* was used to remove eye pigment. We examined the following genotypes: (1, control) *GMR-w-RNAi/+; Vps29^{1}/+*; (2) *GMR-w-RNAi/+; Vps29^{1}/Df*; (3) *GMR-w-RNAi/+; Vps29^{1}*; (4) *GMR-w-RNAi/+; Vps29^{1}/Df; GR/+*. Flies were raised in 12h light/12h dark cycle (L) or in the dark (D). **(C)** Compared with controls (*FRT40A* clones), ERG transient potentials are partially extinguished by rapid stimulation in *Vps35^{MH20}* clones. Clones were generated using *ey-FLP*. Flies were raised in complete darkness and examined at 1-day. (**D**) *Vps35^{MH20}* larval neuromuscular junctions (NMJs) show reduced FM1-43 dye uptake following KCl stimulation, consistent with impaired synaptic vesicle endocytosis. FM1-43 signal intensity (per bouton area) was quantified (n=9-11) in *Vps35^{MH20}* homozygotes or controls (*w*). Statistical analysis based on Student's t-test. All error bars denote SEM. * $p<0.05$.

Figure S2

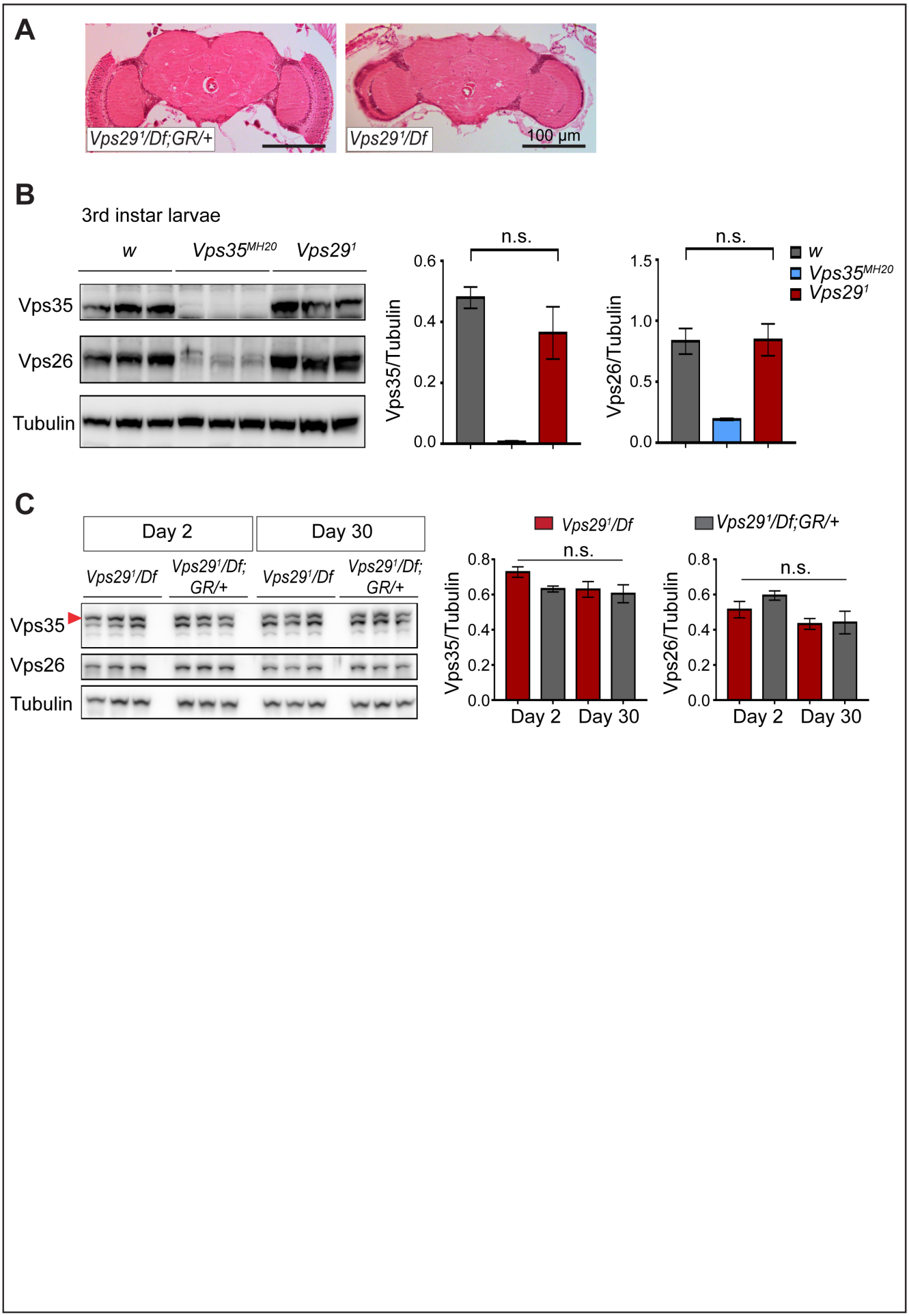

Figure S2 (Related to Figure 3): Loss of Vps29 does not affect Vps35 or Vps26 protein expression.

(**A**) Preserved adult brain histology in aged animals lacking *Vps29*. Hematoxylin and eosin stained frontal sections from 45-day-old $Vps29^{1}/Df$ or control animals ($Vps29^{1}/Df$; *GR/+*) demonstrate no overt neuropathology in the central brain complex. Note that the retina and lamina are absent from frontal sections prepared from *Vps29* mutants from mutant due to severe degeneration of these structures. See also Figure S1B. (**B**) Vps35 and Vps26 protein levels are normally expressed in $Vps29^{1}$ homozygous third instar larvae but absent or reduced, respectively, in $Vps35^{MH20}$ homozygotes. Western blots were probed for Vps35, Vps26, and Tubulin (loading control), and quantified based on n=3 replicate experiments. For statistical analysis, a Student's t-test was performed. (**C**) Vps35 and Vps26 proteins are normally expressed in $Vps29^{1}/Df$ animals. Adult fly head homogenates were prepared from 2-day-old or 30-day-old $Vps29^{1}/Df$ or control animals ($Vps29^{1}/Df$; *GR/+*). Western blots were probed for Vps35, Vps26, and Tubulin (loading control), and quantified based on n=3 replicate experiments. For statistical analysis, one-way ANOVA was performed. Red arrowhead denotes the Vps35-specific band. All error bars denote SEM. n.s., not significant.

Figure S3

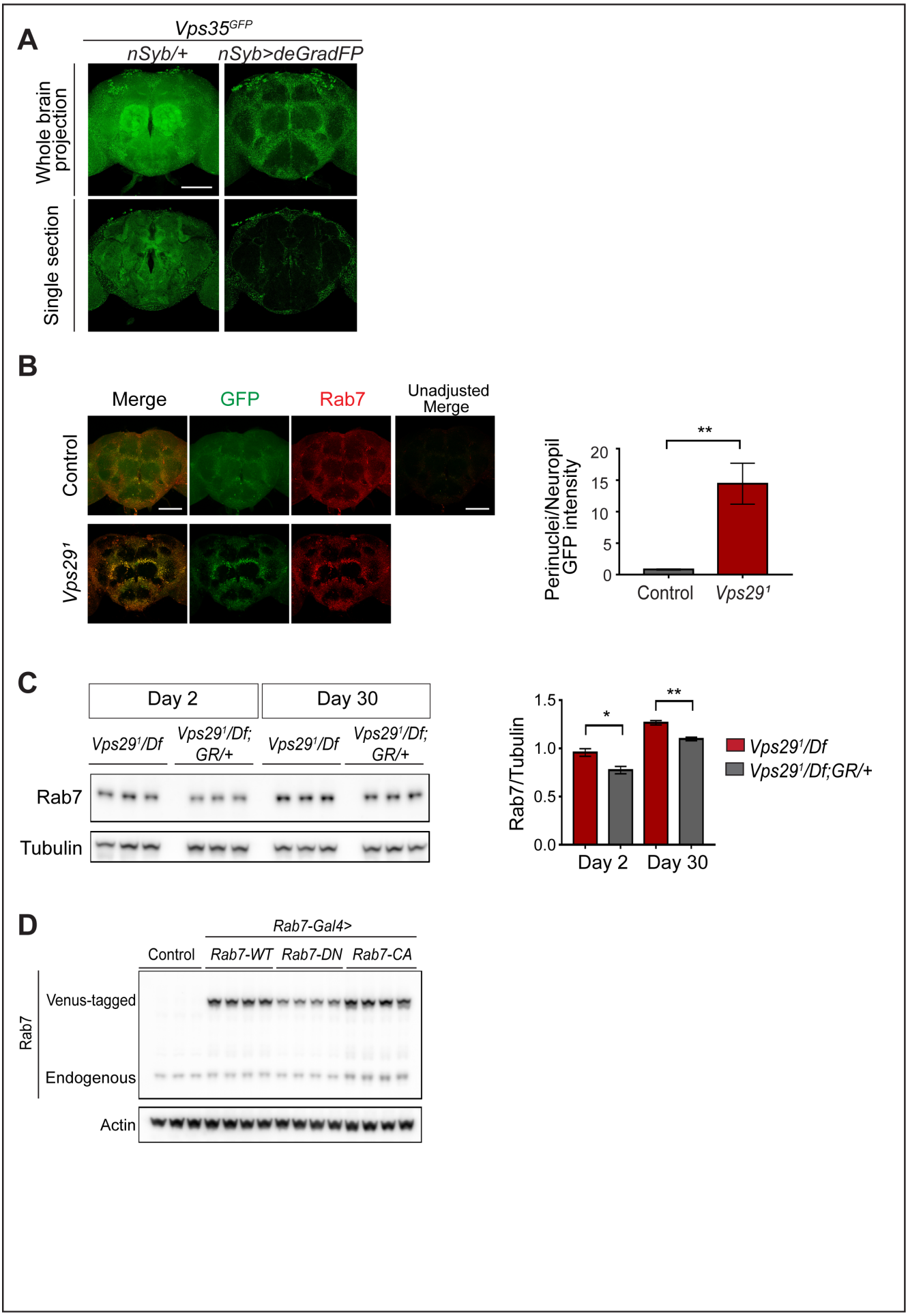

Figure S3 (Related to Figure 4): Loss of Vps29 causes activation and mislocalization of Rab7.

(**A**) Neuronal expression of Vps35 (anti-GFP) in the adult fly brain was examined by selective depletion using deGradFP. The following genotypes were examined: *Vps35^{GFP}; nSyb-Gal4/UAS-deGradFP* (also known as *Nslmb-vhhGFP4*) and *Vps35^{GFP}; nSyb-Gal4/+*. Crosses were established and maintained at 18°C, and adults animals were shifted to 29°C for 7 days post-eclosion, prior to brain dissection. (**B**) In the absence of *Vps29*, Rab7 protein is increased and mislocalized to neuronal soma. *Vps29^{1};Rab7^{EYFP}* homozygotes or control (*Rab7^{EYFP}*) animals, harboring an endogenous, EYFP-tagged Rab7, were stained for Rab7 protein, using both anti-GFP (green) and anti-Rab7 (red). The fluorescence intensity of control animals was amplified for visualization of the weak signal (imaging using consistent settings for controls shown at right). The GFP intensity ratio (perinuclear to neuropil) was quantified (n=4) within antennal lobe region in 2-day-old animals. Scale bars, 100 µm. (**C**) Rab7 protein expression is increased in *Vps29* null animals. Adult fly head homogenates were prepared from 2- and 30-day-old *Vps29^{1}/Df* or controls (*Vps29^{1}/Df; GR/+*). Western blots were probed with anti-Rab7 and anti-Tubulin (loading control), and quantified based on n=3 replicate experiments. **(D)** Western blot showing increased expression of "GTP-locked" *Rab7^{Q67L}* along with corresponding wildtype (*Rab7^{WT}*) and "GDP-locked" (*Rab7^{T22N}*) forms from 5-day-old fly head homogenates prepared from the following genotypes: (1, *Rab7-Gal4>Rab7-CA*) *UAS-Venus-Rab7^{Q67L}/+; Rab7-Gal4/+*; (2, *Rab7-Gal4>Rab7-WT*) *UAS-Venus-Rab7^{WT}/+; Rab7-Gal4/+*; (3, *Rab7-Gal4>Rab7-DN*) *UAS-Venus-Rab7^{T22N}/+; Rab7-Gal4/+*; (4, control) *w*. Western blots were probed for anti-Rab7 and anti-Actin (loading control). Quantification shown in **Figure 4G**. Statistical analysis (**B**, **C**) based on Student's t test. All error bars denote SEM. n.s. not significant; * $p<0.05$; ** $p<0.01$.

Figure S4

A

Cross	Number	CyO	non-CyO	p-Value
Vps29^{GFP}/CyO X *Vps29^{1}*	Observed	222	212	0.6312
	Expected	217	217	
Vps29$^{L152E-GFP}$/CyO X *Vps29^{1}*	Observed	333	249	0.0005
	Expected	291	291	

B

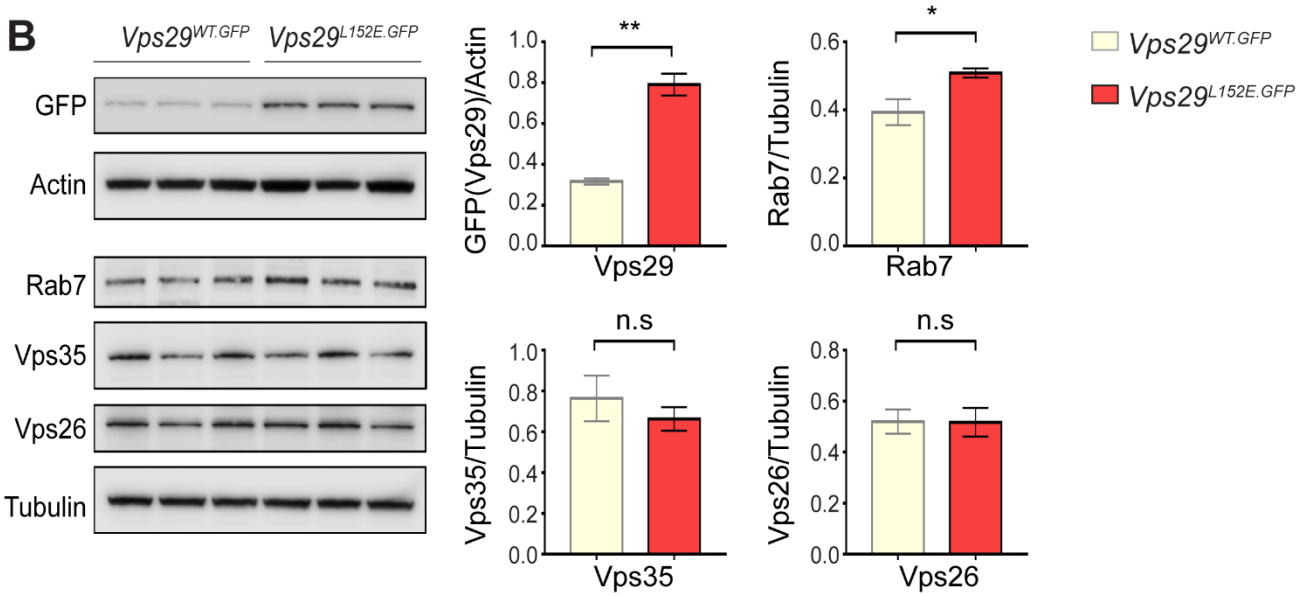

Figure S4 (Related to Figure 5): Additional characterization of the *Vps29^{L152E}*.

(**A**) *Vps29^{L152E}*/*Vps29^{1}* transheterozygotes were recovered at ratios below Mendelian expectations (~43% vs. 50%). For statistical analysis, chi-square test was performed. (**B**) Vps29 (anti-GFP) and Rab7 protein expression are increased in 2-day-old *Vps29$^{L152E.GFP}$* adult heads comparing to controls (*Vps29$^{WT.GFP}$*). Vps35 and Vps26 protein levels were unchanged. Quantification based on n=3 replicate experiments. For statistical analysis, Student's t-test was performed. All error bars denote SEM. n.s. not significant; * $p<0.05$; ** $p<0.01$.

Figure S5

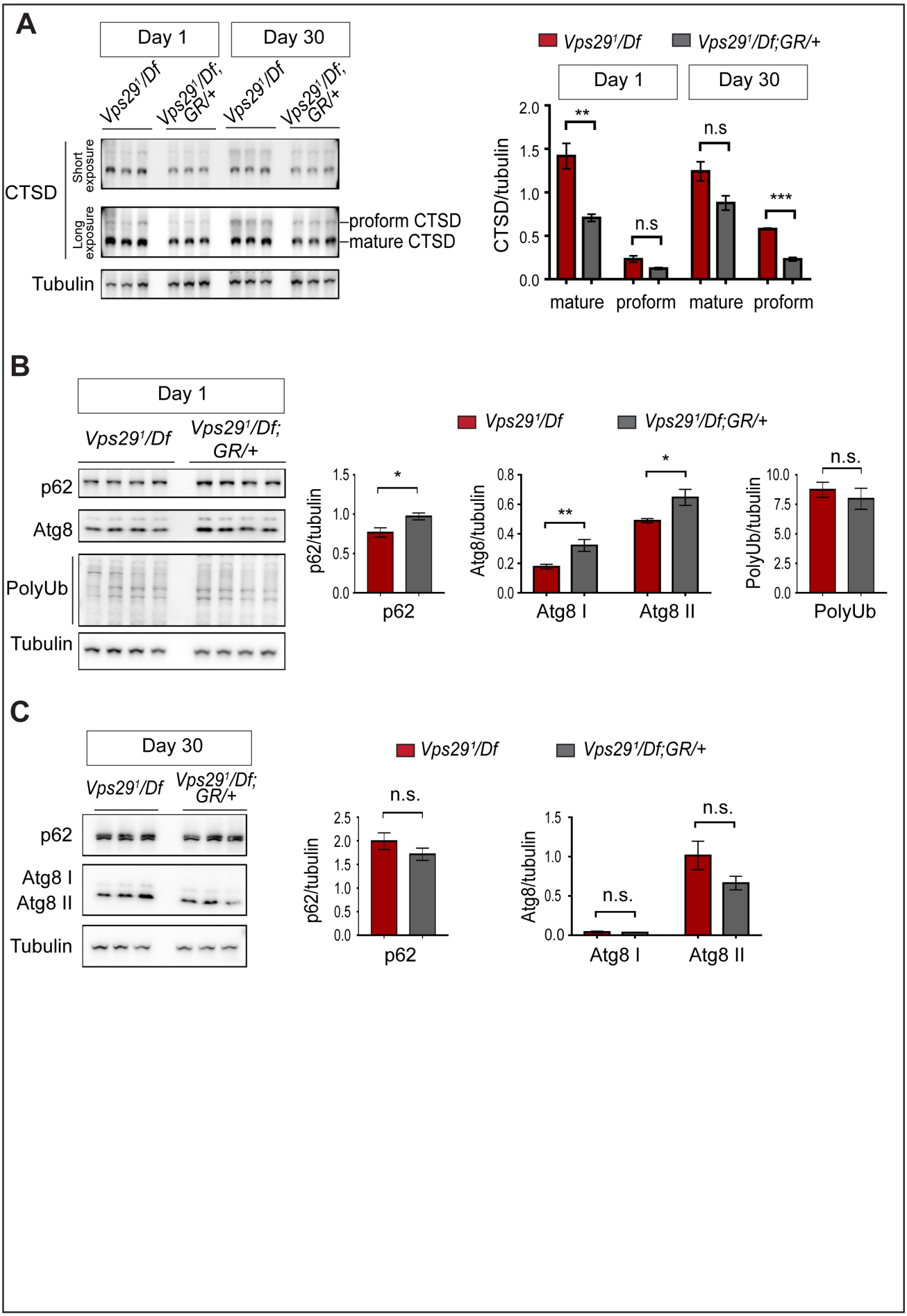

Figure S5 (Related to Figure 6): Additional studies of lysosomal proteolysis and autophagy.

(**A**) The uncleaved CTSD proform is increased in aged animals lacking *Vps29*. Western blots from adult fly head homogenates, including *Vps29*^{1}*/Df* and *Vps29*^{1}*/Df; GR/+* (control), were probed with anti-CTSD, and quantified based on n=3 replicate experiments. **(B, C**) Western blots from fly head homogenates were probed with for p62, Atg8, polyubiquitin (FK1) and Tubulin in 1- (**B**) or 30- (**C**) day-old animals. Quantification based on analysis of n=4 (**B**) or n=3 (**C**) replicate experiments. Statistical analysis (**A-C**) based on Student's t-test. All error bars denote SEM. n.s. not significant. * $p<0.05$; ** $p<0.01$; *** $p<0.001$.

Figure S6

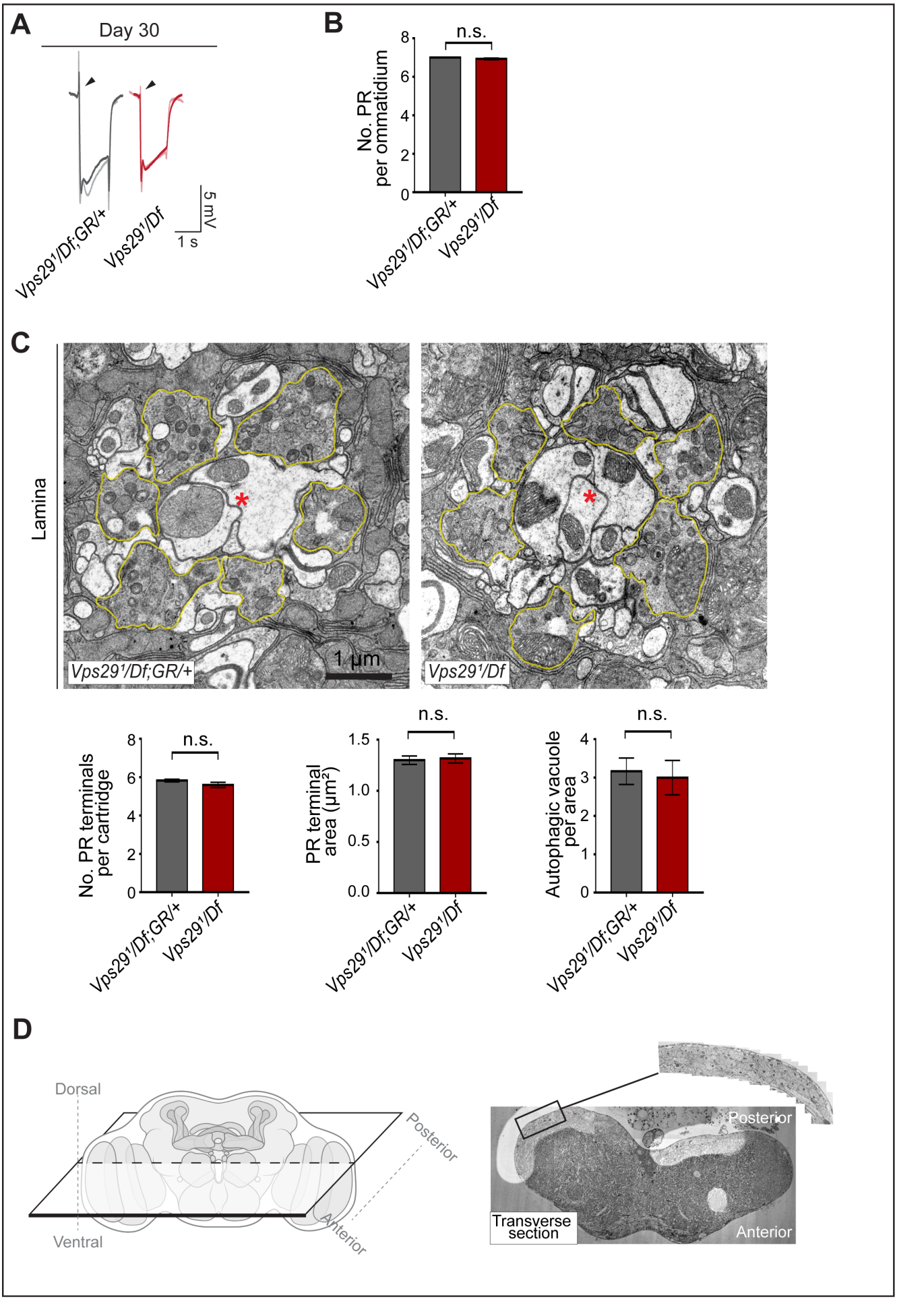

Figure S6 (Related to Figure 7): Additional ultrastructural analysis of *Vps29* mutants.

(**A**) Electroretinogram (ERG) traces of $Vps29^{1}/Df$ and $Vps29^{1}/Df;\ GR/+$ prior to transmission electron microscopy (TEM). Flies were raised under ambient light conditions (~500 lux) for 30 days. Representative traces for n=2 animals are superimposed for each genotype. (**B**) Photoreceptor (PR) numbers are preserved in 30-day-old $Vps29^{1}/Df$ animals, based on counts from retinal TEM. Quantification based on examination of n=30 ommatidia (3 independent animals) for each genotype. (**C**) In 30-day-old *Vps29* mutants, no overt ultrastructural defects are detected in the lamina, which contains PR presynaptic terminals (yellow outline). Dendritic processes (postsynaptic) are indicated with red asterisks. Quantification based on examination of n=30 cartridges (3 independent animals) for each genotype. No detectable changes were in either the number or area of PR terminals or the number of autophagic vacuoles. (**D**) Left: schematic showing orientation for thin sectioning prior to TEM analysis of fly brain. Right: Representative transverse section of fly brain at low magnification. Boxed region of interest (magnified inset) highlights the dorsal-posterior cortical region with densely packed neuronal cell bodies. This was the region imaged at higher magnification in **Figure 7D**. Statistical analysis (**B**, **C**) based on Student's t-test. All error bars denote SEM. n.s. not significant.

Key Resources Table

Reagent type (species) or resource	Designation	Source or reference	Identifiers	Additional information
gene (*D. melanogaster*)	*Vps35*	NA	FLYB: FBgn0034708	
gene (*D. melanogaster*)	*Vps29*	NA	FLYB: FBgn0031310	
gene (*D. melanogaster*)	*Vps26*	NA	FLYB: FBgn0014411	
gene (*D. melanogaster*)	*TBC1D5*	NA	FLYB: FBgn0038129	
gene (*D. melanogaster*)	*Rab7*	NA	FLYB: FBgn0015795	
genetic reagent (*D. melanogaster*)	*FRT40A*	Bloomington *Drosophila* Stock Center	FLYB: FBti000207; RRID: BDSC_1816	y^1 w^{1118}; P{neoFRT}40A
genetic reagent (*D. melanogaster*)	*ey-FLP; FRT40A*	Bloomington *Drosophila* Stock Center	FLYB: FBti0015982; RRID: BDSC_5622	y^{d2}, w^{1118}, ey-FLP,GMR-lacZ;P{neoFRT}40A,w^+,cl/CyO,y+
genetic reagent (*D. melanogaster*)	*$ey^{3.5}$-FLP; FRT40A*	PMID: 15848801	N/A	y w $ey^{3.5}$-FLP; FRT40A,cl, w^+/CyO, Kr>GFP
genetic reagent (*D. melanogaster*)	*nSyb-Gal4*	Bloomington *Drosophila* Stock Center	FLYB: FBti0150361; RRID: BDSC_51635	y^1 w*; P{nSyb-GAL4.S}3
genetic reagent (*D. melanogaster*)	*nos-Cas9*	Bloomington *Drosophila* Stock Center	FLYB: FBti0159183; RRID: BDSC_54591	y^1, w*,M{nos-Cas9.P}ZH-2A
genetic reagent (*D. melanogaster*)	*$Vps35^{MH20}$/CyO*	Bloomington *Drosophila* Stock Center	FLYB: FBal0221635; RRID: BDSC_67202	w; P{neoFRT}42D,$Vps35^{MH20}$/CyO, Kr>GFP
genetic reagent (*D. melanogaster*)	*Df*	Bloomington *Drosophila* Stock Center	FLYB: FBti0073468; RRID: BDSC_7491	Df(2L)Exel6004
genetic reagent (*D. melanogaster*)	*UAS-deGradFP*	Bloomington *Drosophila* Stock Center	FLYB: FBti0147362; RRID: BDSC_38421	w*; P{w[+mC]=UAS-Nslmb-vhhGFP4}3
genetic reagent (*D. melanogaster*)	*GMR-w-RNAi*	Bloomington *Drosophila* Stock Center	FLYB: FBti0074622; RRID: BDSC_32067	GMR-w-$RNAi^{13D}$
genetic reagent (*D. melanogaster*)	*$Vps35^{GFP}$*	This study	N/A	Progenitor = w; $Vps35^{TagRFP-T}$; TagRFP-T cassette was replaced by EGFP
genetic reagent (*D. melanogaster*)	*$Vps35^{RFP}$*	PMID: 26700726	N/A	w; $Vps35^{TagRFP-T}$
genetic reagent (*D. melanogaster*)	*eyFLP;FRT42D*	PMID: 24781186	N/A	y w,eyFLP,GMR-lacZ; P{neoFRT}42D,w^+,cl/CyO,Kr>GFP
genetic reagent (*D. melanogaster*)	*UAS-Vps35*	PMID: 24781186	N/A	y w; PBac{UAS-Vps35-HA}
genetic reagent (*D. melanogaster*)	*$Rab7^{EYFP}$*	Bloomington *Drosophila* Stock Center	FLYB: FBst0062545 RRID: BDSC_62545	w^{1118}; TI{TI}$Rab7^{EYFP}$
genetic reagent (*D. melanogaster*)	*$Rab7^{Gal4\text{-}KO}$/TM3,Sb*	PMID: 24327558	FLYB: FBal0294205	FRT82B, $Rab7^{Gal4\text{-}KO}$/TM3,Sb

genetic reagent (D. melanogaster)	*UAS-Venus-Rab7^{Q67L}/CyO*	PMID: 24327558	FLYB: FBal0294206	*PBac{UAS-Rab7.Q67L.Venus}*
genetic reagent (*D. melanogaster*)	*UAS-Venus-Rab7^{T22N}/CyO*	PMID: 24327558	FLYB: FBal0294207	*PBac{UAS-Rab7.T22N.Venus}*
genetic reagent (*D. melanogaster*)	*UAS-Venus-Rab7^{WT}/CyO*	PMID: 24327558	FLYB: FBal0294208	*PBac{UAS-Rab7.WT.Venus}*
genetic reagent (*D. melanogaster*)	*Vps29^{1}/CyO,twi-GFP*	This study	N/A	fly strain carrying the *ywing^{2+}* dominant marker replacing the gene *Vps29*
genetic reagent (*D. melanogaster*)	*Vps29$^{WT.GFP}$/CyO,ubi-GFP*	This study	N/A	fly strain carrying the *Vps29* gene with EGFP…(GGS)4 sequence inserted at the N-terminus of Vps29
genetic reagent (*D. melanogaster*)	*Vps29$^{L152E.GFP}$/CyO,ubi-GFP*	This study	N/A	fly strain carrying the *Vps29* gene with EGFP…(GGS)4 sequence inserted at the N-terminus of Vps29. L152 amino acid is mutated to E
genetic reagent (*D. melanogaster*)	*Vps29-GR*	This study	N/A	CH322-128G03 (FLYB: FBcl0761727)
genetic reagent (*D. melanogaster*)	*UAS-dVps29*	This study	N/A	*y w; PBac{UAS-dVps29-myc}*
genetic reagent (*D. melanogaster*)	*UAS-hVps29-1*	This study	N/A	*y w; PBac{UAS-hVps29-1-FLAG}*
genetic reagent (*D. melanogaster*)	*UAS-hVps29-2*	This study	N/A	*y w; PBac{UAS-hVps29-2-FLAG}*
genetic reagent (*D. melanogaster*)	*UAS-hVps29-3*	This study	N/A	*y w; PBac{UAS-hVps29-3-FLAG}*
genetic reagent (*D. melanogaster*)	*UAS-dTBC1D5*	This study	N/A	*y w; PBac{UAS-dTBC1D5-myc}*
genetic reagent (*D. melanogaster*)	*w; FRT40A, Vps29^{1}/CyO*	This study	N/A	
genetic reagent (*D. melanogaster*)	*w;Vps29^{1},Vps35^{GFP}/CyO*	This study	N/A	
genetic reagent (*D. melanogaster*)	*w;Vps29^{1}/CyO; Vps29-GR/TM6B*	This study	N/A	
genetic reagent (*D. melanogaster*)	*w;Vps29^{1}/CyO; Rab7^{EYFP}/TM6B*	This study	N/A	
genetic reagent (*D. melanogaster*)	*w;Vps29^{1}/CyO; nSyb-Gal4/TM6B*	This study	N/A	
genetic reagent (*D. melanogaster*)	*w;Vps29^{1}/CyO; UAS-dVps29/TM6B*	This study	N/A	
genetic reagent (*D. melanogaster*)	*w;Vps29^{1}/CyO; UAS-hVps29/TM6B*	This study	N/A	
genetic reagent (*D. melanogaster*)	*w;Vps29^{1}/CyO;UAS-dTBC1D5/TM6B*	This study	N/A	
genetic reagent (*D. melanogaster*)	*w;Vps29^{1}/CyO;UAS-dVps35/TM6B*	This study	N/A	
antibody	FITC-conjugated anti-GFP (mouse monoclonal)	Santa Cruz Biotechnology	Cat# sc-9996 FITC; RRID: AB_627695	1:100 for IF
antibody	anti-Rab7 (mouse monoclonal)	Developmental Studies Hybridoma Bank	RRID: AB_2722471	1:100 for IF; 1:1000 for WB
antibody	anti-Elav (Rat monoclonal)	Developmental Studies Hybridoma Bank	DSHB: Elav-7E8A10; RRID: AB_528218	1:500 for IF

antibody	anti-tubulin Clone DM1A (mouse monoclonal)	Sigma Aldrich	Cat# T6199; RRID: AB_477583	1:1000 for WB
antibody	anti-Vps29 (goat polyclonal)	LifeSpan Biosciences	Cat# LS-C55674; RRID: AB_2214913	1:2000 for WB
antibody	anti-Vps35 (Guinea pig polyclonal)	This study	N/A	against C-terminal 338 amino acids of fly Vps35; 1:2000 for WB
antibody	anti-Vps26 (Guinea pig polyclonal)	PMID: 24781186	N/A	1:2000 for WB
antibody	anti-CTSL (mouse monoclonal)	R&D Systems	Cat# MAB22591; RRID: AB_2087830	1:1000 for WB
antibody	anti-CTSD (goat polyclonal)	Santa Cruz Biotechnology	Cat# sc-6487; RRID: AB_637895	1: 500 for WB
antibody	Rabbit anti-Atg8	PMID: 27068460	N/A	1:1000 for WB
antibody	Anti-Polyubiquitinylated conjugates Clone FK1 (mouse monoclonal)	Enzo Life Sciences	Cat# BML-PW8805-0500; RRID: AB_2052280	1:1000 for WB
antibody	Rabbit anti-p62/Ref(2)p	PMID: 25686248	N/A	1:2000 for WB
antibody	anti-actin clone C4 (mouse monoclonal)	Millipore	Cat# MAB1501; RRID: AB_2223041	1:1000 for WB
antibody	Cy3-conjugated anti-HRP	Jackson ImmunoResearch	Cat# 123-165-021; RRID: AB_2338959	1:150 for IF
antibody	Cy3-conjugated Goat anti-mouse IgG	Jackson ImmunoResearch	Cat# 115-165-146; RRID: AB_2338690	1:500 for IF
antibody	Cy3-conjugated Goat anti-Rat IgG	Jackson ImmunoResearch	Cat# 112-165-003; RRID: AB_2338240	1:500 for IF
antibody	Mouse anti-goat IgG-HRP	Santa Cruz Biotechnology	Cat# sc-2354, RRID: AB_628490	1:5000 for WB
antibody	Goat anti-mouse IgG-HRP	Santa Cruz Biotechnology	Cat# sc-2005; RRID: AB_631736	1:5000 for WB
antibody	Goat anti-rabbit IgG-HRP	Santa Cruz Biotechnology	Cat# sc-2004; RRID: AB_631746	1:5000 for WB
antibody	Rabbit anti-Glc-Cer	Glycobiotech	Cat# RAS_0010	1:250 for IF
recombinant DNA reagent	Plasmid: pUASTattb_dVps29-myc	This study	N/A	Progenitors: GH25884 (cDNA)
recombinant DNA reagent	Plasmid: pUASTattb_dTBC1D5-myc	This study	N/A	Progenitors: BS16827 (cDNA)
recombinant DNA reagent	Plasmid: pUASTattb_hVps29-1-FLAG	This study	N/A	Progenitors: OHu00442D (cDNA)
recombinant DNA reagent	Plasmid: pUASTattb_hVps29-2-FLAG	This study	N/A	Progenitors: OHu02289D (cDNA)
recombinant DNA reagent	Plasmid: pUASTattb_hVps29-3-FLAG	This study	N/A	Progenitors: OHu05688D (cDNA)
commercial assay or kit	Subcloning Efficiency DH5α competent cells	Thermo Fisher Scientific	Cat# 18265017	
commercial assay or kit	Q5 Site-Directed Mutagenesis Kit	NEB	Cat# E0554S	

commercial assay or kit	NEBuilder HiFi DNA Assembly Cloning Kit	NEB	Cat# E5520S	
commercial assay or kit	PureLink Genomic DNA Kits	Thermo Fisher Scientific	Cat# K182001	
commercial assay or kit	GFP-Trap agarose beads	Allele Biotechnology	Cat# ABP-NAB-GFPA100	
chemical compound, drug	2X Laemmli Sample Buffer	Bio-Rad	Cat# 161-0737	
chemical compound, drug	4% paraformaldehyde in 1XPBS	ChemCruz	Cat# sc-281692	
chemical compound, drug	RapiClear	SunJin Lab Co.	N/A	
chemical compound, drug	Vectashield	Vector Laboratories	Cat# H-1000	
chemical compound, drug	Protein A/G agarose	Thermo Fisher	Cat# 20421	
chemical compound, drug	8% glutaraldehyde	EMS	Cat# 16020	
chemical compound, drug	Cacodylic Acid, Trihydrate Sodium 100g	EMS	Cat# 12300	
chemical compound, drug	EM-grade glutaraldehyde, 25% Aq solution	EMS	Cat# 16221	
chemical compound, drug	Osmium tetroxide 4% Aq solution	EMS	Cat# 19191	
chemical compound, drug	Paraformaldehyde 16% Aq Solution	EMS	Cat# 15711	
chemical compound, drug	Propylene Oxide	EMS	Cat# 20411	
chemical compound, drug	Koptec 200 Proof 100% ethanol Anhydrous	VWR	Cat# 89125-186	
chemical compound, drug	Embed-812	EMS	Cat# 14901	
chemical compound, drug	NMA	EMS	Cat# 19001	
chemical compound, drug	DDSA	EMS	Cat# 13711	
chemical compound, drug	DMP-30	EMS	Cat# 13600	
chemical compound, drug	Uranyl Acetate	EMS	Cat# RT22400	
chemical compound, drug	Lead Nitrate	EMS	Cat# RT17900-25	
chemical compound, drug	Phalloidin 488 nm	ThermoFisher	Cat# AB_2315147	
chemical compound, drug	FM 1-43FX	Invitrogen	Cat# F35355	
chemical compound, drug	Western Lightning Plus-ECL	PerkinElmer	Cat# 121001EA	
software, algorithm	Leica Application Suite X	Leica	RRID:SCR_013673	
software, algorithm	LabChart Reader	ADInstruments	https://www.adinstruments.com/products/labchart-reader; RRID: N/A	
software, algorithm	ImageJ	National Institute of Health	RRID:SCR_003073	

Sequence-based reagent	dVps29-myc-F	N/A	N/A	5'-GAAGATCTTCATGCTCGTTCTGGTACTCGGCGA-3'
Sequence-based reagent	dVps29-myc-R	N/A	N/A	5'-GCTCTAGACTACAGATCCTCTTCTGAGATGAGTTTTTGTTCGATCTTCTTGTACTCGATGCGCTCCA-3'
Sequence-based reagent	dTBC1D5-myc-F	N/A	N/A	5'-GAAGATCTATCAACATGACTGTTTGGGGAATAGAAGCCATCA-3'
Sequence-based reagent	dTBC1D5-myc- R	N/A	N/A	5'-GCTCTAGATCACAGATCCTCTTCTGAGATGAGTTTTTGTTCACTCGATTCGTTTCGATGCCGT-3'
Sequence-based reagent	hVps29-1-F	N/A	N/A	5'-CCGCCTCGAGGCCACCATGTTGGTGTTGGT-3'
Sequence-based reagent	hVps29-2-F	N/A	N/A	5'-CCGCCTCGAGGCCACCATGGCTGGGCACA-3'
Sequence-based reagent	hVps29-3-F	N/A	N/A	5'-CCGCCTCGAGGCCACCATGAGCAGGTGTGCT-3'
Sequence-based reagent	hVps29-R	N/A	N/A	5'-CTAGTCTAGATTATCACTTATCGTCGTCATCCTTGTAATCAGGT-3'
Sequence-based reagent	Vps29-P1-F	N/A	N/A	5'-GAACCTGACGTATCCGGAGC-3'
Sequence-based reagent	Vps29-P1-R	N/A	N/A	5'-TCGCCGATCAGTTGGTACAC-3'
Sequence-based reagent	Vps29-P2-F	N/A	N/A	5'-CTCGTTCTGGTACTCGGCG-3'
Sequence-based reagent	Vps29-P2-R	N/A	N/A	5'-ACGAACGAAGGCACCACATT-3'
Sequence-based reagent	Vps29-P3-F	N/A	N/A	5'-GGCCGCATACATCACATCCT-3'
Sequence-based reagent	Vps29-P3-R	N/A	N/A	5'-GAATTTGTTGCCGTGCTCGT-3'
Sequence-based reagent	Vps35-F (Internal control)	N/A	N/A	5'-TTGTACCTCCTCATAACAGTGGG-3'
Sequence-based reagent	Vps35-R (Internal control)	N/A	N/A	5'-TCGTTCTCCTCAACCATCACAT-3'
Other	Leica SP8 confocal microscope	Leica	N/A	

Other	Leica DM 6000 B system	Leica	N/A	
Other	Zeiss LSM 880 with Airyscan	Zeiss	N/A	